AD-A050 785   RCA LABS PRINCETON N J   F/G 20/12
RADIATION EFFECTS ON THE ELECTRICAL PROPERTIES OF MOS DEVICE MA--ETC(U)
FEB 78 G W HUGHES   DAAG39-76-C-0088
UNCLASSIFIED   PRRL-77-CR-37   HDL-CR-77-088   NL

1 OF 1
AD
A050785

END
DATE
FILMED
4-78
DDC

HDL-CR-77-088

12

RADIATION EFFECTS ON THE ELECTRICAL PROPERTIES OF MOS DEVICE MATERIALS

HDL-CR-77-088, *Radiation Effects on the Electrical Properties of MOS Device Materials,* by Gary W. Hughes

FEBRUARY 1978

Prepared by

RCA Laboratories
Princeton, NJ 08540

Under Contract

DAAG39-76-C-0088

This work was sponsored by the Defense Nuclear Agency under Nuclear Weapons Effects Research Subtask Z99QAXTA007 (Transient Radiation Effects Physics), Work Unit 61 (Surface Effects and Interface State Investigations).

U.S. Army Materiel Development
and Readiness Command
HARRY DIAMOND LABORATORIES
Adelphi, Maryland 20783

UNCLASSIFIED
SECURITY CLASSIFICATION OF THIS PAGE (When Data Entered)

(19) **REPORT DOCUMENTATION PAGE**		**READ INSTRUCTIONS BEFORE COMPLETING FORM**
1. REPORT NUMBER (18) HDL-CR-77-088	2. GOVT ACCESSION NO.	3. RECIPIENT'S CATALOG NUMBER (9) Final rept. 2 Mar 76-28 Feb 77,
4. TITLE (and Subtitle) (6) RADIATION EFFECTS ON THE ELECTRICAL PROPERTIES OF MOS DEVICE MATERIALS.		5. TYPE OF REPORT & PERIOD COVERED Final Report (3-2-76 to 2-28-77)
		6. PERFORMING ORG. REPORT NUMBER (14) PRRL-77-CR-37
7. AUTHOR(s) (10) Gary W. Hughes		8. CONTRACT OR GRANT NUMBER(s) DAAG39-76-C-0088 DRCMS Code: 697000.22 MIPR 76-654
9. PERFORMING ORGANIZATION NAME AND ADDRESS RCA Laboratories Princeton, NJ 08540		10. PROGRAM ELEMENT, PROJECT, TASK AREA & WORK UNIT NUMBERS Prog Element: 6.27.04 Subtask: Z99QAXTA007 HDL Project: 236628
11. CONTROLLING OFFICE NAME AND ADDRESS Defense Nuclear Agency Washington, DC 20305		12. REPORT DATE (11) Feb[redacted]978
		13. NUMBER OF PAGES 71 (12) 63p.
14. MONITORING AGENCY NAME & ADDRESS (if different from Controlling Office) Harry Diamond Laboratories 2800 Powder Mill Rd Adelphi, MD 20783		15. SECURITY CLASS. (of this report) Unclassified
		15a. DECLASSIFICATION/DOWNGRADING SCHEDULE N/A

16. DISTRIBUTION STATEMENT (of this Report)

(15) DAAG39-76-C-0088,
DNA-MIPR-76-654

Approved for public release; distribution unlimited.

17. DISTRIBUTION STATEMENT (of the abstract entered in Block 20, if different from Report)

(16) Z99QAXT
(17) A007

18. SUPPLEMENTARY NOTES

This work was sponsored by the Defense Nuclear Agency under Nuclear Weapons Effects Research Subtask Z99QAXTA007 (Transient Radiation Effects Physics), Work Unit 61 (Surface Effects and Interface State Investigations).

19. KEY WORDS (Continue on reverse side if necessary and identify by block number)

SiO_2, MOS, CMOS
Radiation Hardness
Interface States
Capture Cross Sections
Vacuum Ultraviolet Radiation

20. ABSTRACT (Continue on reverse side if necessary and identify by block number)

Radiation-hard SiO_2 on Si grown by three different processes (dry, pyrogenic steam, and hybrid) has been examined by vacuum ultraviolet techniques. Flatband shift vs time measurements provide estimates of capture cross sections and trap densities. Current-enhancement measurements provide qualitative information about trapping at both the $Si-SiO_2$ and gate-SiO_2 interface.

DD FORM 1 JAN 73 1473

UNCLASSIFIED
SECURITY CLASSIFICATION OF THIS PAGE (When Data Entered)

299 000 JOB

20.

Results show that unannealed dry oxides have the lowest interface-state density after irradiation, making them more desirable for applications where switching speed is important. Annealing in argon at 800°C increases both the hole-trap and interface-state density. All dry oxides have a dominant trap with capture cross section S $\simeq$ ~~5×10^{-14}~~ cm^2 at applied oxide fields E_o = 1 MV/cm. E sub o

Pyrogenic steam oxides have many more interface states after irradiation than dry oxides and can be characterized by a dominant trap with S $\simeq$ * ~~$5 \times 10^{-14} - 10^{-13}$~~ cm^2 for E_o = 1 MV/cm. Oxides annealed at 900°C have the smallest density of hole traps.

Hybrid oxides grown in 3% HCl steam followed by dry O_2 show S $\sim$ ** ~~2×10^{-13}~~ cm^2 at E_o = 1 MV/cm. The larger capture cross section for these oxides is believed to be due to the presence of HCl.

All oxides show a neutral trap capture cross section which is approximately inversely proportional to applied oxide field. Both pyrogenic steam and dry hard oxides can be characterized by the same trap. The difference between the two oxides appears to be only the density of interface states.

approx. =

5 x 10 to the -14th power sq cm

* 5 x 10 to the -14th power to 10 to the -13th power sq. cm.

** 2 x 10 to the -13th power sq. cm

PREFACE

This final report, prepared by RCA Laboratories, Princeton, NJ 08540, under Contract DAAG39-76-C-0088, describes work performed principally in the Solid State Technology Center, J. H. Scott, Jr., Director.

The Project Supervisor is K. H. Zaininger, and the Project Scientist is G. W. Hughes. Device processing and radiation testing were performed with the competent assistance of M. Morad. R. Snedeker, and F. Taft. The assistance of J. Fabula and S. Cohen, RCA Solid State Technology Center, Somerville, NJ, in fabricating the hybrid oxides is greatly appreciated.

CONTENTS

Section Page

FIGURES

FIGURES (Continued)

FIGURES (Continued)

1. INTRODUCTION

The growth of radiation-hard SiO_2 for MOS integrated circuits is now within the capability of the semiconductor industry. In spite of this, however, a complete understanding of the basic degradation problem is not yet in hand. Recently work has been reported which illuminates the mechanism of hole transport in SiO_2,[1-3] but an understanding of the atomic and chemical nature of the hole trap and radiation-induced interface state in SiO_2 is far from complete.

Several models of hole traps have been proposed based upon the short range order of SiO_2 and band structure considerations. DiStephano and Eastman[4] used photoemission spectroscopy to examine the valence-band structure of SiO_2 and found a narrow band of states near the valence-band edge which they attributed to oxygen non-bonding orbitals. Sigel et al. showed that SiO_2 films exhibit an E' center during electron spin resonance measurements which they believe is due to oxygen vacancies near the Si-SiO_2 interface.[5] Sah believes that hole traps are primarily interstitial oxygen vacancies and trivalent silicons.[6] It is also possible that some hole traps and interface states are caused by impurity species within the SiO_2. This is

---

[1] *J. R. Srour, S. Othmer, O. L. Curtis, Jr., and K. Y. Chiu, IEEE Trans. Nucl. Sci. NS-23, 1513 (1976).*

[2] *F. B. McLean, H. E. Boesch, Jr., and J. M. McGarrity, IEEE Trans. Nucl. Sci. NS-23, 1506 (1976) and H. E. Boesch, Jr., F. B. McLean, J. M. McGarrity, and G. A. Ausman, Jr., IEEE Trans. Nucl. Sci. NS-22, 2163 (1975).*

[3] *R. C. Hughes, Bull. Am. Phys. Soc. 21, 404 (1976).*

[4] *T. H. DiStephano and D. E. Eastman, Sol. State Comm. 9, 2259 (1971).*

[5] *G. H. Sigel, Jr., E. J. Friebele, R. J. Ginther, and D. L. Griscom, IEEE Trans. Nucl. Sci. NS-21, 56 (1974).*

[6] *C. T. Sah, IEEE Trans. Nucl. Sci. NS-23, 1563 (1976).*

supported by the many observations that show the difficulty of fabricating consistently hard oxides with a given process.[7,8]

Whatever the nature of hole traps may be, it is clear that they are very process-dependent. For those traps that are deep enough to prevent thermal detrapping, a knowledge of the capture cross section and trap density is sufficient to characterize the radiation response of the oxide. In this report we have measured capture cross sections and trap densities for many different process variations in order to try to understand the process dependence of radiation-hard oxides.

The characterization of hard oxides is usually determined by a flatband or threshold voltage shift after a certain radiation dose, typically 10^6 rad. While the voltage shift thus measured is usually assumed to be due mainly to oxide trapped charge, there is evidence to suggest that radiation-induced interface states may play a role that is equally important. It is possible that these interface states may be largely responsible for the wide variation in radiation sensitivity of thermal SiO_2 grown under similar process conditions.[9] Our recent work in fact shows that hard oxides can be grown in dry oxygen at temperatures ranging from 900° to 1050°C.[9] In the past it has been assumed that 1000°C was optimum. This conclusion may have resulted from an occurrence of large numbers of post-irradiation interface states in the oxides grown at other temperatures.

The role that interface states and oxide traps play in determining radiation sensitivity can only be determined by a technique that can separate the two effects. Recently Ning and Yu[10] reported a

---

[7] *B. L. Gregory, IEEE Trans. Nucl. Sci.* NS-22, *2295 (1975).*

[8] *G. W. Hughes and R. J. Powell, IEEE Trans. Nucl. Sci.* NS-23, *1569 (1976).*

[9] *G. W. Hughes, "Radiation and Charge Transport in SiO_2," Final Report prepared under Contract N00014-74-C-0185 for Office of Naval Research, July 1977.*

[10] *T. H. Ning and H. N. Yu, J. Appl. Phys.* 45, *5373 (1974).*

method for studying electron traps in SiO_2 which has been used by Aitken et al.[11] to measure electron capture cross sections and trap densities of thermal SiO_2. In this technique, the measured flatband voltage shift of an MOS capacitor as a function of time during electron injection is used to derive the capture cross section S and trap density N_T of oxide traps. This technique was also developed independently by R. J. Powell for capture of holes during the first two quarters of this contract. In addition to this method Powell has developed a current-enhancement technique which gives information about hole traps at both the Si-SiO_2 and gate-SiO_2 interface.[12] This current-enhancement phenomenon proves to be a very sensitive measure of the number and location of traps near the Si-SiO_2 and gate-SiO_2 interfaces. Furthermore, it provides a tool for comparing radiation sensitivity between samples with different processing histories. Both of the above techniques have been used here in a slightly modified form to draw conclusions about the nature of hole traps in SiO_2 grown by different processes. The processes that we have examined are: (1) dry oxides grown at temperatures from 900° to 1150°C; (2) pyrogenic steam oxides grown at 875°C and annealed between 900° and 1100°C; and (3) pyrogenic hybrid oxides grown at 925°C and annealed between 925° and 1150°C.

Section 2 discusses the model used for the trapping kinetics of holes in SiO_2, the effects of interface states on measured flatband voltage shifts, and the high field current-enhancement phenomenon. Section 3 discusses the sample preparation techniques and the methods by which the trapping parameters were measured. Section 4 presents the experimental results and makes interpretations about the nature of trapping and interface-state generation from the flatband shift and current-enhancement data. Finally, Section 5 summarizes and concludes with some observations and suggestions for future work.

---

[11] *J. M. Aitken, D. J. DiMaria, and D. R. Young, IEEE Trans. Nucl. Sci.* *NS-23*, *1526 (1976).*

[12] *R. J. Powell, J. Appl. Phys.* *46*, *4557 (1975).*

2. HOLE TRAPPING IN SiO_2

2.1 Trapping Kinetics

Consider a distribution of traps in a narrow region near the $Si\text{-}SiO_2$ interface. Let there be N_T traps per cm^2 of which N_T^+ traps per cm^2 are filled with holes. Then the trapping probability of a hole reaching the interface is $(N_T - N_T^+)\,S$, where S is the capture cross section for holes. Letting J be the constant hole current density flowing through the interface, we can write:

$$\frac{dN_T^+}{dt} = \frac{J}{q}\,(N_T - N_T^+)\,S \tag{1}$$

This equation has the solution:

$$N_T^+ = N_T \left(1 - e^{\frac{-JSt}{q}}\right) \tag{2}$$

and if we express the densities of traps in terms of flatband shift, equation (2) becomes:

$$\Delta V_{FB} = \Delta V_{FBF} \left(1 - e^{\frac{-JSt}{q}}\right) \tag{3}$$

where $\Delta V_{FB} = \left(qN_T^+ d_{ox}\right)/\varepsilon_{ox}$ is the flatband shift at time t, d_{ox} is the oxide thickness, ε_{ox} is the dielectric constant, and $\Delta V_{FBF} = \left(qN_T d_{ox}\right)/\varepsilon_{ox}$ is the flatband shift with all the traps filled. This simple model assumes that emission from traps is unimportant. One can determine the trap density N_T and the capture cross section S by fitting equation (3) to experimental data. Unfortunately, it is not always possible to measure ΔV_{FBF} directly because tunnel injection may prevent complete filling of traps, and the highest value of ΔV_{FB} reached may be appreciably less than ΔV_{FBF}. More importantly, radiation-induced interface states at saturation can account for a substantial amount of positive or negative charge making a determination of N_T from ΔV_{FBF} difficult.

There are several alternate ways of determining N_T and S from the data. Consider the derivative of equation (3):

$$\frac{d}{dt}\Delta V_{FB} = \Delta V_{FBF}\, e^{\frac{-JSt}{q}} \left(\frac{JS}{q}\right) \tag{4}$$

Equation (4) at t = 0 gives the product $N_T S$, e.g.,

$$\left|\frac{d}{dt}\Delta V_{FB}\right|_{t=0} = \Delta V_{FBF}\,\frac{JS}{q} = J\,\frac{d_{ox}}{\varepsilon_{ox}}\,(N_T S) \tag{5}$$

Also taking the log of equation (4) gives

$$\ell n\left[\frac{d}{dt}\Delta V_{FB}\right] = \ell n\left[\frac{Jd_{ox}}{\varepsilon_{ox}}\,(N_T S)\right] - \frac{JS}{q}\,t \tag{6}$$

Therefore the slope of equation (6) on a semi-log plot yields the capture cross section S. This technique is also limited to situations in which interface-state charge is a small fraction of oxide-trapped charge, that is, early in the irradiation. For hard oxides in which the amount of oxide-trapped charge is small, this may mean measuring many flatband shifts to a high degree of accuracy during the first few seconds of exposure.

Another alternative which gives less precise results but makes measurements more feasible is to use equation (5) to determine the product $N_T S$ and then extract N_T from ΔV_{FBF} by putting upper and lower bounds on it. This can be done by measuring the flatband voltage at two points where either all the acceptor or all the donor interface states are charged.

2.2 Effect of Interface States on Measured Flatband Voltage

Consider the band diagram shown in figure 1(a). The surface is in accumulation and the Fermi level is at the conduction band edge. All acceptor interface states will be charged negatively as shown and all donors will be neutral. Thus, the total flatband shift

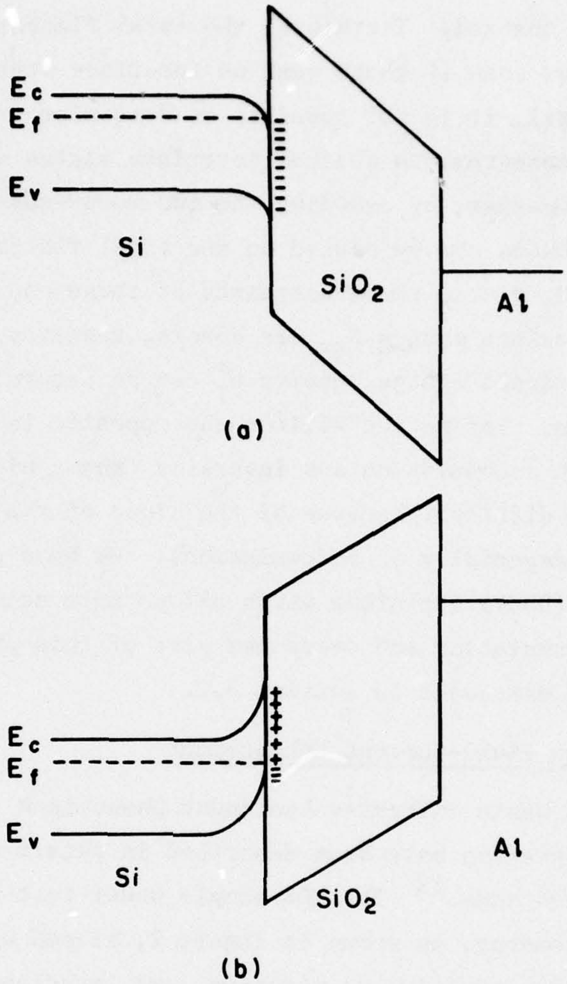

Figure 1. Band diagram of $Si-SiO_2$ MOS capacitor. (a) In accumlation, only acceptor interface-state charged; (b) in inversion, mostly donors are charged.

ΔV_{FB} will be more positive than if there were no interface states (oxide charge is positive). On the other hand, if the silicon surface is inverted as shown in figure 1(b), the Fermi level is near the valence-band edge, all donors above the Fermi level will be charge, and all acceptors neutral. Between the Fermi level and the valence band the opposite situation will prevail, but as a first-order estimate *mostly* donors will be charged. Therefore, the total flatband shift ΔV_{FB} will be more negative than if there were no interface states present.

In general, it is not possible to determine from capacitance-voltage (C-V) measurements whether interface states are donors or acceptors.[13] However, by assuming the two worst-case situations outlined above, bounds can be placed on the total flatband shift and we can determine N_T within the constraints of these bounds. For example, if all the interface states N_{SS} are donors, then for n-type silicon the actual oxide-trapped charge density N_T^+ can be determined by measuring ΔV at inversion. For p-type silicon the opposite is of course true. Measuring ΔV at accumulation and inversion from a high-frequency C-V (HFCV) plot is difficult because of the slope of the C-V curves at these points (especially at accumulation). We have devised a deep-depletion C-V (DDCV) technique which allows more accurate measurement of ΔV_{FB} at accumulation and overcomes part of this problem. This method will be discussed in section 3.2.

2.3 High Field-Current Enhancement

The basic current-enhancement phenomenon and its experimental implementation have been described in detail elsewhere and will only be outlined here.[12] The MOS sample under test is placed in a vacuum monochromator, as shown in figure 2, biased with an appropriate gate bias, either positive or negative, and irradiated with vacuum ultraviolet (VUV) light of a photon energy that is strongly absorbed* in the oxide film. The time dependence of the total current flowing through the MOS device is measured. The current measured at the initiation of radiation is just the electron or hole photocurrent flowing through the oxide. If the applied field is sufficient, eventually a

---

[13] *G. W. Hughes, J. Appl. Phys. 48, 5357 (1977).*

**This is not essential, and the device may be irradiated with penetrating radiation as well.*

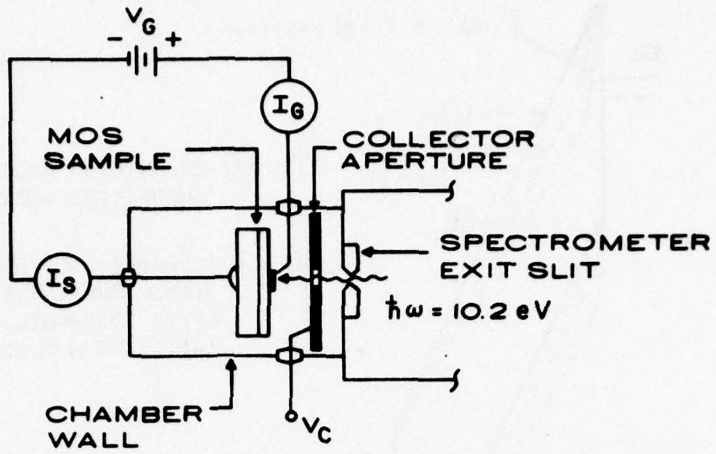

Figure 2. Experimental arrangement used for hole transport studies.

current enhancement will be observed as holes accumulate near the negatively biased electrode, and the interface field increases enough to allow Fowler-Nordheim tunneling of electrons to occur. The mechanism of current enhancement is depicted schematically in figures 3 and 4. Figure 3 shows the band diagram for SiO_2 as irradiation progresses. Initially the field throughout the SiO_2 is approximately the applied field, which must be $\gtrsim 5$ MV/cm for current enhancement to occur. This is to ensure that any holes trapped at the Al interface do not perturb the field there enough to decrease the net hole generation through geminate recombination. During this time the net hole generation is constant, and the measured photocurrent does not change with time as figure 4 shows. As the density of trapped holes builds up at the silicon interface, the bands bend as shown in figure 3 until the barrier becomes thin enough for tunneling to occur. At this point, marked ① in figure 4, the total current increases as more holes are trapped and the bands are bent even further, resulting in even more tunneling current. In the absence of interface states, this situation continues until equilibrium is reached when the number of holes trapped per unit time is just balanced by the number annihilated by the tunneling electrons. This is marked ② in figure 4 as the current approaches

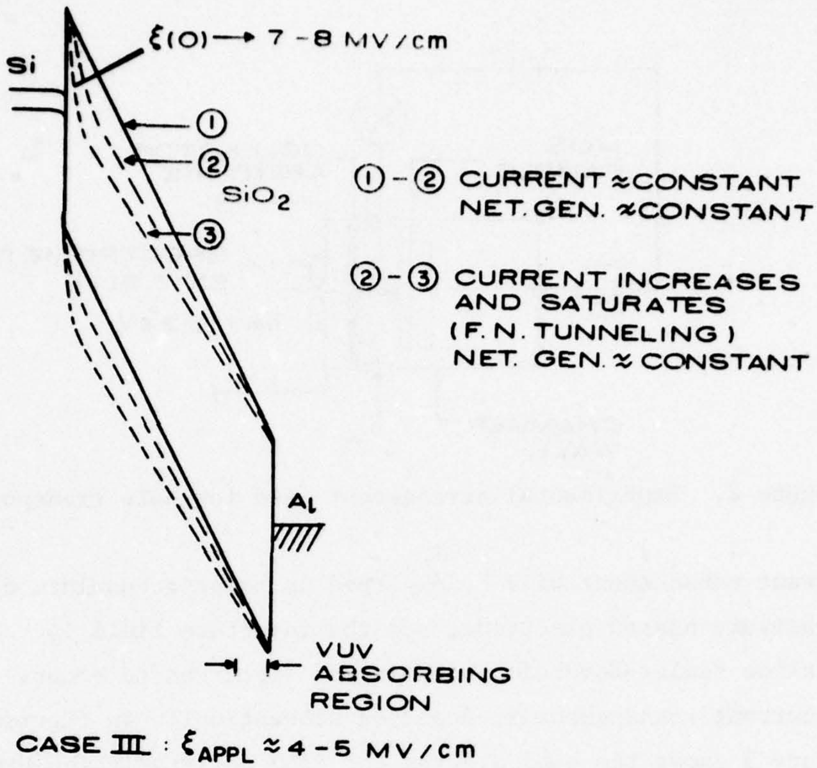

Figure 3. Energy band diagram of an Si-SiO$_2$ MOS structure with high applied field.

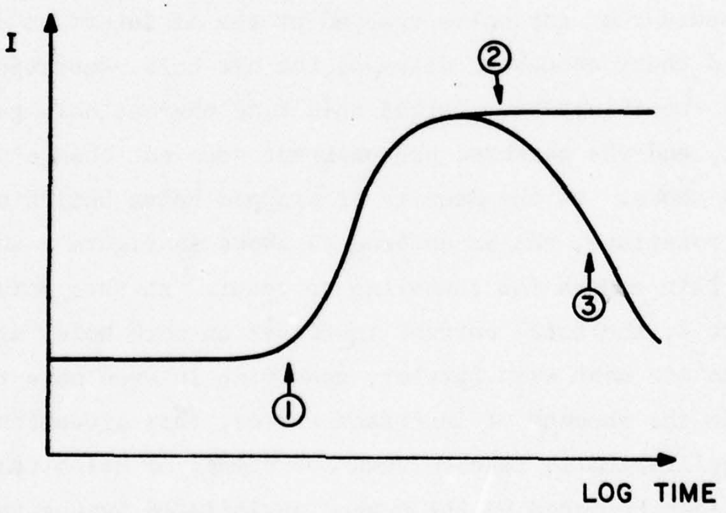

Figure 4. Behavior of measured current vs time under bias conditions shown in fig. 3. Numbers refer to discussion in text.

saturation. In some samples, instead of saturating, the current actually begins to decrease as time goes on. One might speculate that this is due to a decrease in the net number of trapped holes as electrons tunneling in from the silicon annihilate them. However, this would have a self-limiting effect since as the net hole density decreases, the interface field and hence the tunneling current would decrease until equilibrium was reached. Actually, equilibrium would be established before the current had a chance to decrease and situation ② would prevail. The most probable explanation for this decreasing current phenomenon is that acceptor-type interface states are generated near the interface and partially compensate the field enhancement due to hole trapping. This hypothesis is illustrated in figure 5. Here we show the band diagram at the Si-SiO_2 interface under three different conditions. Condition I shows the SiO_2 conduction band edge under an oxide field of 5 MV/cm with no oxide charge or interface states. Condition II includes a positive sheet of oxide charge of 5×10^{12} cm^{-2} 50 Å from the Si-SiO_2 interface, and condition III includes both the positive oxide charge and a negative sheet of interface states 10 Å from the interface of the same magnitude as the oxide charge. The location and magnitude of the positive charge is reasonable and is based upon measurements of charge centroids[11,14] and our current-enhancement data. The location of the interface-state centroid at 10 Å from the silicon interface is not unreasonable especially for midgap states.[15] The magnitude of this charge is based upon the deep-depletion C-V measurements shown below.

---

[14] *R. J. Powell and G. W. Hughes, "Radiation and Charge Transport in SiO_2," Annual Report prepared under Contract N00014-74-C-0185 for Office of Naval Research, January 1975.*

[15] *F. P. Heiman and G. Warfield, IEEE Trans. Electron. Devices ED-12, 167 (1965).*

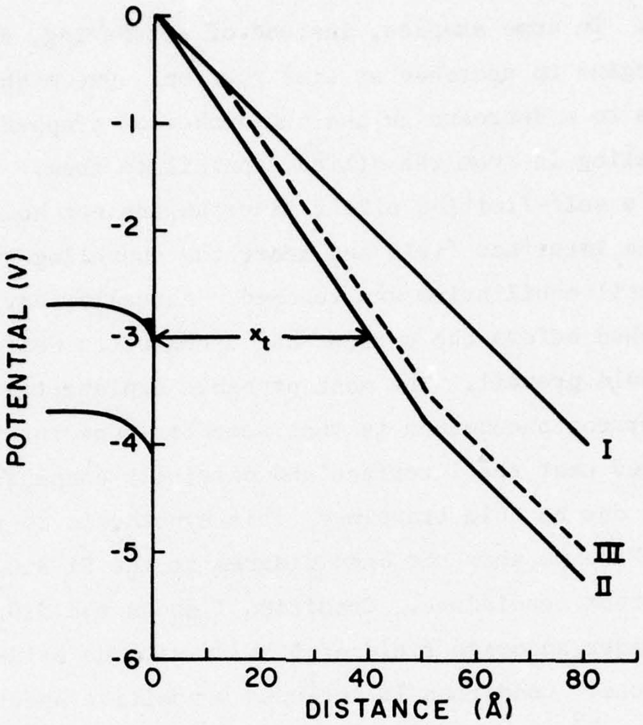

Figure 5. Band diagram of Si-SiO$_2$ MOS interface showing the effect of positive and negative sheet on band bending and tunneling distance. Roman numerals refer to discussion in text.

In condition I, no current enhancement results because the tunneling distance $x_t \simeq 60$ Å. In condition II, the positive sheet charge increases the interfacial field to 7.5 MV/cm, and decreases the tunneling distance to 40 Å allowing large enhancement currents to flow. In condition III, the negative interface-state charge compensates the positive oxide charge and the tunneling distance x_t increases to $\simeq$42 Å. Since the tunneling current depends exponentially upon barrier width, this results in a decrease in current by at least an order of magnitude.[12]

Current enhancement is also a very useful tool for probing the hole traps at the Al-SiO$_2$ interface where there is no counterpart to flatband shift measurements. The current enhancement at this interface is solely a function of the applied field and trap density. Interface states do not exist here, so that the interpretations are simplified. In section 4.2 we present some interesting results using this technique.

3. EXPERIMENTAL METHODS

3.1 Sample Preparation

Oxide films were thermally grown on n- and p-type 5 to 10 ohm-cm (100) silicon slices by three different processes. These processes are summarized in table I.

TABLE I. PROCESSING CONDITIONS

Oxidation Process	Oxidation Temperature (°C)	Anneal Temp (15 min)	Nominal Oxide Thickness (Å)
Dry (p-type)	900 1000 1150	Half annealed in Ar at 800°C, half unannealed	750
Pyrogenic Steam (100%) (n-type)	875	900°C to 1100°C in He	1000
Hybrid (30-min 100% pyrogenic with 3% HCl steam 60-min dry O_2 (n-type))	925	925°C *in situ* in N_2	750

Pyrogenic steam is nothing more than steam produced by burning hydrogeninside the furnace tube. With adjustment of the ratio of H_2 to O_2, the steam content can be varied from 0 to 100%. The advantages of this method are (1) the percentage steam can be controlled accurately, (2) the purity of the steam is determined solely by the purity of the gases, and (3) the steam can be quickly and easily shut on and off, making hybrid oxides possible.

All of these wafers were metallized with 1-mm-diameter semitransparent aluminum dots approximately 100 Å thick. The aluminum was evaporated from an In Source® induction-heated crucible source and in all cases resulted in less then 0.1-V shift under a standard bias-temperature C-V test (CVBT; ±10 V at 300°C for 5 min).

For comparison purposes all wafers used in the capture cross-section study were also irradiated with 1-MeV electrons under 1-MV/cm positive bias to a dose of 10^6 rad. The results of this test are shown in figures 6, 7, and 8. All flatband shifts are normalized by a square law thickness dependence to 750 Å. As the figures show, some of the oxides are relatively hard and some of them, not being grown by an optimum process, are very soft. This wide range of radiation sensitivities is desirable in that it provides us with a wide range of process-induced trapping situations for study. The inclusion of a hard oxide from each of the three processes also provides us with a benchmark for comparison of the other oxides.

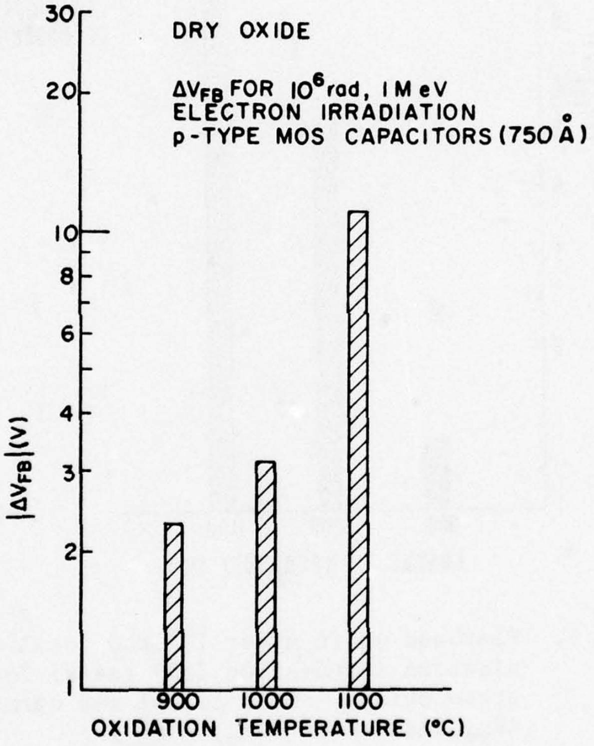

Figure 6. Flatband shift after 10^6 rad total dose 1-MeV electron irradiation (10^4 rad/s) for dry oxides.

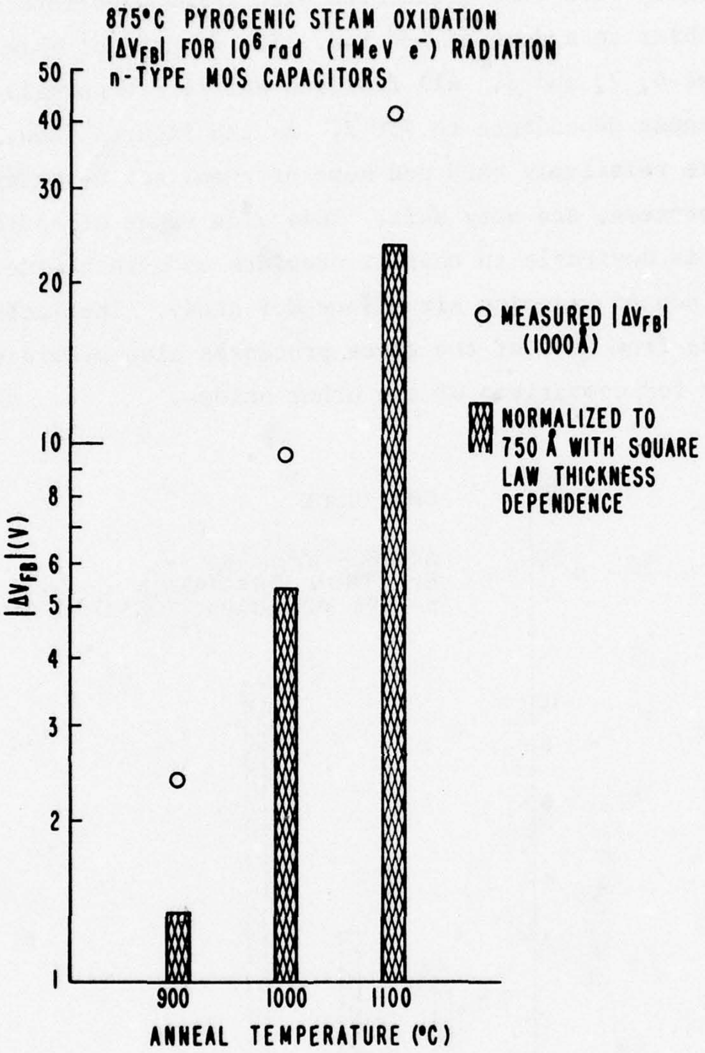

Figure 7. Flatband shift after 10^6 rad total dose 1-MeV electron irradiation (10^4 rad/s) for pyrogenic steam oxides. Both actual and normalized ΔV_{FB} data shown ($\Delta V_{FB} \propto d_{ox}^2$).

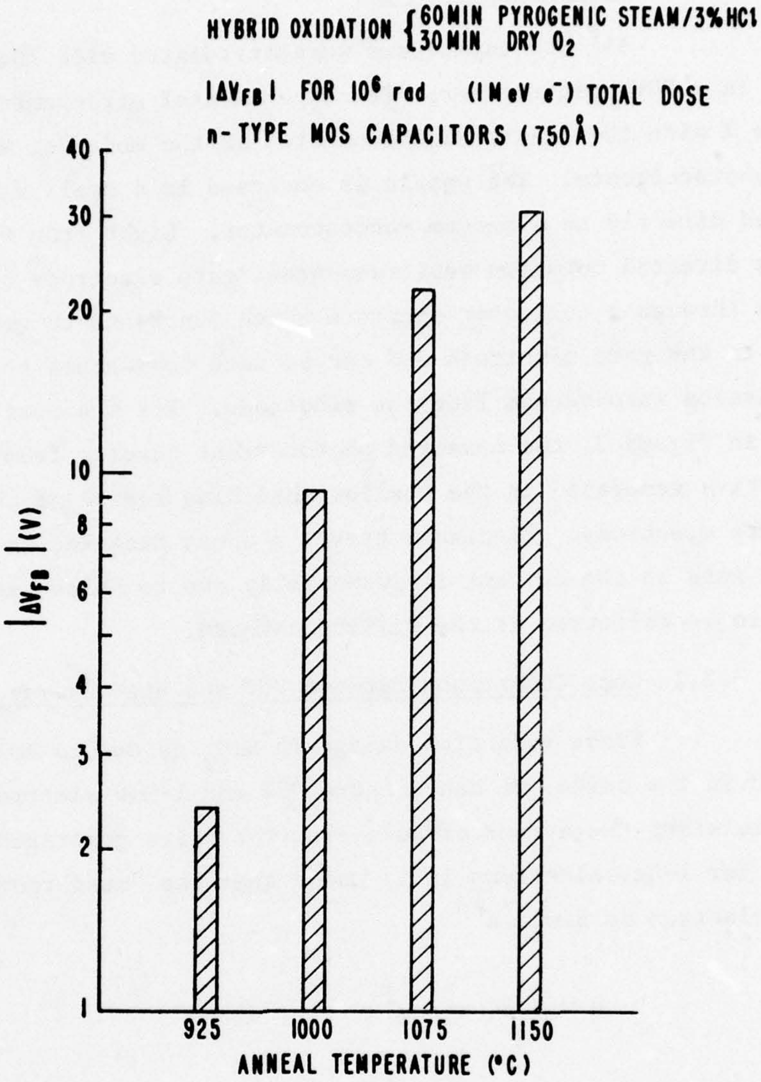

Figure 8. Flatband shift after 10^6 rad total dose 1-MeV electron irradiation (10^4 rad/s) for hybrid oxides.

3.2 Measurement Techniques

3.2.1 Hole Photocurrents

All MOS capacitors were irradiated with 10.2-eV VUV light in a VUV spectrometer. The experimental arrangement is shown in figure 2 with the electronics connected in the mode for measuring the hole photocurrents. The sample is enclosed in a small vacuum chamber coupled directly to a vacuum monochromator. Light from the monochromator is directed onto the semitransparent gate electrode of the MOS sample through a collector aperture which functions to confine the light to the gate electrode and can be used to measure the magnitude of emission into vacuum from the electrode. For the bias polarity shown in figure 3, the measured photocurrent results from electron-hole pairs generated in the shallow absorbing region of the SiO_2 near the gate electrode. Electrons travel a short distance to be collected at the gate so the current is essentially due to holes traversing the oxide to be collected at the silicon cathode.

3.2.2 Dose Comparison Between VUV and High Energy Irradiation

Since radiation damage in SiO_2 is due to holes being trapped in the oxide, we can compare VUV and 1-MeV electron irradiation by calculating the number of hole-electron pairs generated per second.

For 1-MeV electrons it is known that the "mean range" of a 1-MeV electron is SiO_2 is[16]

$$R = 3.84 \text{ mg/cm}^2 \tag{9}$$

The density of SiO_2 is 2.3 g/cm^3 so that the actual absorption depth is

$$L_A = 0.169 \text{ cm} \tag{10}$$

---

[16] *L. Katz and A. S. Penfold, Rev. of Modern Physics* 24, *28 (1952).*

Defining $\beta = \frac{L_A}{E_s}$ where $E_s = 1$ MeV, then,

$$\beta = 1.69 \times 10^{-7} \text{ cm/eV} \tag{11}$$

Assuming a pair formation energy E_p, the length required to create one electron-hole pair is βE_p. The total number of electron-hole pairs/cm^2 created in an oxide of thickness d_{ox} after a dose of Φ rad is then

$$N_p = \alpha \Phi \frac{d_{ox}}{\beta E_p} \tag{12}$$

where $\alpha = 3 \times 10^{-7}$ MeV electrons/cm^2/rad.

Srour et al.[17] have estimated $E_p \simeq 19$ eV. Therefore, for a 750-Å-thick oxide and a dose of 10^6 rad,

$$N_p = 6.96 \times 10^{13} \text{ cm}^{-2} \tag{13}$$

For VUV irradiation, Powell has shown that the initial hole photocurrent and thus the quantum yield Y saturates with Y near 100% as the oxide field approaches 5 MV/cm because of the reduction of geminate recombination.[12]

For the light intensity and electrode area that we use, we find the hole photocurrent at 5 MV/cm is typically

$$J_{ph} \simeq 5.1 \times 10^{-8} \text{ A/cm}^2 \tag{14}$$

Thus, the number of electron-hole pairs created by the VUV per cm^2 per second is

$$\frac{J_{ph}}{q} = 3.18 \times 10^{11} \text{ s}^{-1} \text{ cm}^{-2} \tag{15}$$

The total number for t in seconds is then

$$N_p = \frac{J_{ph}}{q} t \tag{16}$$

---

[17] *J. R. Srour, O. L. Curtis, and K. Y. Chiu, IEEE Trans. Nucl. Sci. NS-21, 73 (1974). For analysis of data in preceding reference, see G. A. Ausman, Jr. and F. B. McLean, Appl. Phys. Letters 26, 173 (1975).*

So from equation (13) and (16) we find t $\underset{\sim}{}$ 218 s for an equivalent 1-Mrad VUV dose.

3.2.3 Deep-Depletion C-V Measurements

Flatband shifts during irradiation were measured by both a high-frequency C-V (HFCV) technique and a deep-depletion C-V (DDCV) technique. In the high-frequency technique, the capacitor is irradiated for a length of time at a positive bias, the radiation is removed, and a 1-MHz HFCV curve is taken. The whole procedure takes about 20 s. In the DDCV technique, a bias is applied during the irradiation as shown in figure 9. With a small sampling resistor, R_S, the current is calculated by measuring the voltage $V_S(t)$ as shown in figure 9. When a DDCV measurement is desired, the bias is rapidly swept down to a preset negative voltage and back, the whole sweep taking about 100 μs. During this time the UV can be either on or off as it does not affect the measurement. The method is similar to a quasi-static C-V measurement except that the sweep rate of the ramp voltage is very high. Under steady-state conditions, the capacitor is biased far into accumulation at $+V_B$. At the moment the DDCV curve is needed, a high sweep-rate negative-going ramp is initiated which sweeps to $-V_I$ and then retraces at the same rate back to $+V_B$. If α is the sweep rate of the ramp, then, neglecting R_S, the current through the capacitor is

$$I = C(V_g) \frac{dV_g}{dt} = \alpha C(V_g) \tag{17}$$

and

$$V_S = IR_S = \alpha R_S C(V_g) \tag{18}$$

Time is related to V_g through the relationship $V_g = \alpha t$ so that the time scale can be quickly converted to a voltage scale.

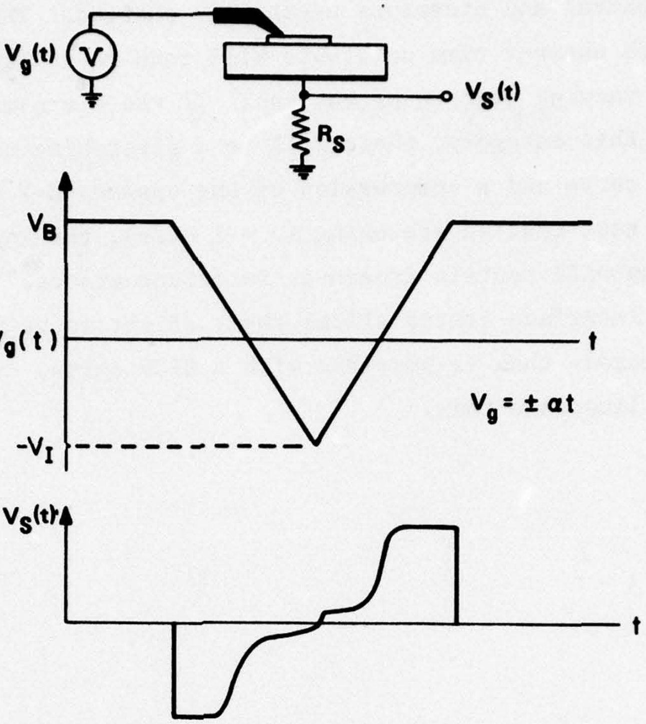

Figure 9. Deep-depletion C-V measurement technique showing circuit connections and voltage waveforms.

Without interface states, the above system gives an accurate replica of a deep-depletion C-V curve. The majority carriers are in equilibrium with the ramp voltage as long as the sweep time is long compared with the geometrically modified dielectric-relaxation time of the MOS capacitor.[18] The minority carriers are "frozen-out" for moderate to high slew rates. When interface states are present, the response of the capacitor is slightly different. Interface states with time constants long compared with the sweep time will be "frozen in" with the Fermi level at the conduction band point. That is, donors

---

[18] *G. W. Hughes and R. M. White, IEEE Trans. Electron. Devices* *__ED-22__, 945 (1975).*

will be neutral and acceptors negatively charged. Those interface states with shorter time constants will tend to follow the voltage ramp with varying degrees of success. If there are many interface states in this category, there will be a stretching out of the downsweep C-V curve and a compression of the upsweep C-V curve.[19] For the sweep rate that we are using (α = 1 MV/s), the lower 0.7 eV of the bandgap will contain frozen-in interface states.[20] This freezing-in of the interface states allows their effect to be measured much more accurately than is possible with a HFCV curve. The data in section 4.1 illustrate this.

---

[19] *J. G. Simmons and L. S. Wei, Solid State Electronics* *16*, *53 (1973).*

[20] *S. M. Sze, Physics of Semiconductor Devices (John Wiley & Sons, New York, 1969), p. 455.*

4. MEASURED HOLE CAPTURE CROSS SECTION AND TRAP DENSITIES

4.1 Interpretation of ΔV_{FB} vs t Data

Using the techniques described in section 3, we irradiated MOS capacitors on the oxides shown in table I and measured the flat-band shifts as a function of time. From these data, the capture cross section and trap density were determined.

At the beginning of the irradiation the initial probability of capture P_{co} is given by

$$P_{co} = N_T S \tag{19}$$

From equation (5) this is

$$P_{co} = \frac{C_{ox}}{I_o} \frac{d}{dt} \left[\Delta V_{FB}\right]_{t=o} \tag{20}$$

where C_{ox} is the actual oxide capacitance and I_o is the initial photo-current.

For $t \ll q/JS$, equation (3) shows that

$$\Delta V_{FB} \sim \frac{I_o}{C_{ox}} P_{co} t \tag{21}$$

This equation can safely be used to measure P_{co} directly as long as the measured ΔV_{FB} versus t is linear in t. For example, in our experiments it is difficult to determine exposures accurately for less than 1 s, and it becomes increasingly difficult to resolve small flat-band shifts for very short exposures. Consequently, our measurement technique consists of the following procedure. The sample is exposed for 1 s, a DDCV curve taken, the sample allowed to relax for 60 s, and a DDCV curve is taken again. This allows any transporting charge to move completely through the oxide. The sample is exposed again for another 1 s and the whole process repeated. An example of the resulting flatband shifts before and after relaxation is shown in figure 10. This is an 875°C pyrogenic oxide annealed at 900°C in helium. The bias during irradiation is +5 MV/cm. (This particular bias was used during most of the measurements because it is the bias needed to interpret the current enhancement data.) The probability of capture was measured for other biases and was found to be bias-dependent. This will be discussed below. This particular sample had about 0.04-V shift due solely to transporting charge which disappeared after the capacitor was allowed to relax. Other samples showed less of a discrepancy between the initial and relaxed ΔV_{FB}. Note also that the slope of ΔV_{FB} versus t is 1.0 on a log-log scale which validates the assumptions made for equation (21). From this figure and equation (21), we find $P_{co} = N_T S = 0.02$.

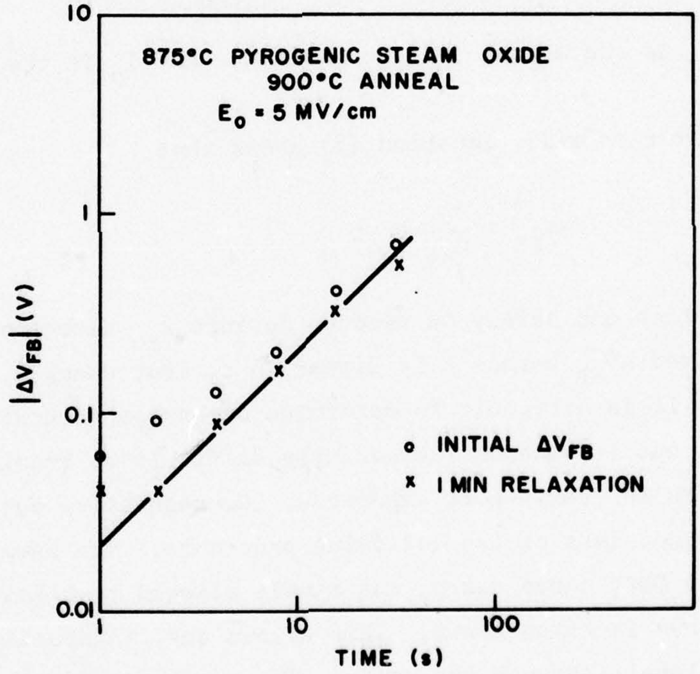

Figure 10. Initial $|\Delta V_{FB}|$ vs t data for pyrogenic steam oxide annealed at 900°C, showing relaxation effect and resulting unity slope line.

After the probability of capture is measured, what remains to be determined is N_T or S from the ΔV_{FB} versus t data. As explained above, because of the relative inaccuracy in our measurement technique, it is not possible to use equation (6) to measure the capture cross section S. Instead, we measured ΔV versus t by both HFCV and DDCV techniques and determined bounds on ΔV_F from these measurements. Figure 11 shows these measurements for the same sample as in figure 10. This figure contains three sets of data, the DDCV data measured from accumulation (+5 MV/cm), and the HFCV data measured at flatband and inversion. As the figure shows, for t $\gtrsim$ 250 s, the DDCV curve begins to deviate from the HFCV curve and eventually reverses. The deviation between the curves shows that interface states are being created between the flatband Fermi level and silicon conduction band. However, it is not possible to determine whether these states are donors or acceptors.[13] The reversal of the DDCV curve implies one of two things. (1) The oxide trapped charge N_T^+ is being annihilated by electrons tunneling in from the silicon under high fields (see fig. 3). This must be accompanied by an increase in the number of donor interface states above the flatband Fermi level E_F which must compensate both the annihilated N_T^+ *and* all acceptor N_{SS} below E_F. (2) The net oxide-trapped charge N_T^+ does *not* decrease with time but the number of acceptor N_{SS} throughout the bandgap increases and becomes greater than N_T^+ (see section 2.2).

For the reasons given in section 2 we believe the second scenario is the most probable one, but in either case the reversal can be used to set a lower bound on N_T, the number of fillable traps. The Fermi level is at the conduction band when the DDCV measurement is initiated, so that in either case only acceptor interface states are charged and ΔV_{FB} due to N_T is at least as large as the maximum shown.

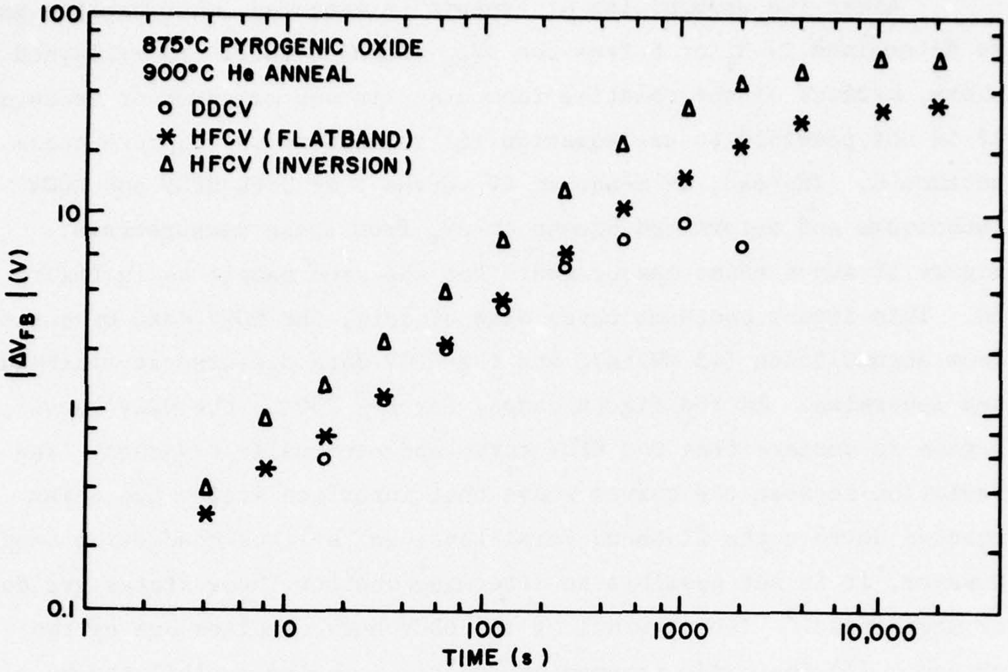

Figure 11. Complete $|\Delta V_{FB}|$ vs t data for pyrogenic steam oxide annealed at 900°C showing differences between DDCV and HFCV techniques. 5-MV/cm bias.

The upper limit on N_T is of course determined by the saturated C-V shift at inversion. Here the Fermi level is near the silicon valence band, all the donors above E_F are charged positively, and any acceptors between E_V and E_F are charged negatively. Presumably, the net interface charge in this case would be positive. This being the case, the ΔV due to N_T, the number of fillable traps, is no larger than that measured at inversion.

These two cases give us limits on N_T through the equation

$$N_T = \frac{\varepsilon_{ox}}{qd_{ox}} |\Delta V_F| \tag{22}$$

where ε_{ox} and d_{ox} are the permittivity and thickness of the SiO_2 and q is the magnitude of the electronic charge. From the upper and lower limit on N_T, lower and upper limits on S can be computed from equation (19). This was done for some of the oxides shown in table I for applied oxide fields E_o of 1, 3, and 5 MV/cm. The data from these measurements are shown in appendix A. The results of the capture cross section and trap density calculations are shown in figures 12, 13, and 14 for E_o = 1 MV/cm. While capture cross-section data do not provide any definitive answers about the nature of hole traps, such data can be useful for comparing oxides of different degrees of hardness. For the oxides grown for this study, the degree of hardness ranges from very hard to very soft depending upon the particular process used. It would be useful then to know if the capture cross sections for the very hard and very soft oxides are quite different, suggesting a different hole trap, or if they are the same, suggesting perhaps only a difference in trap density.

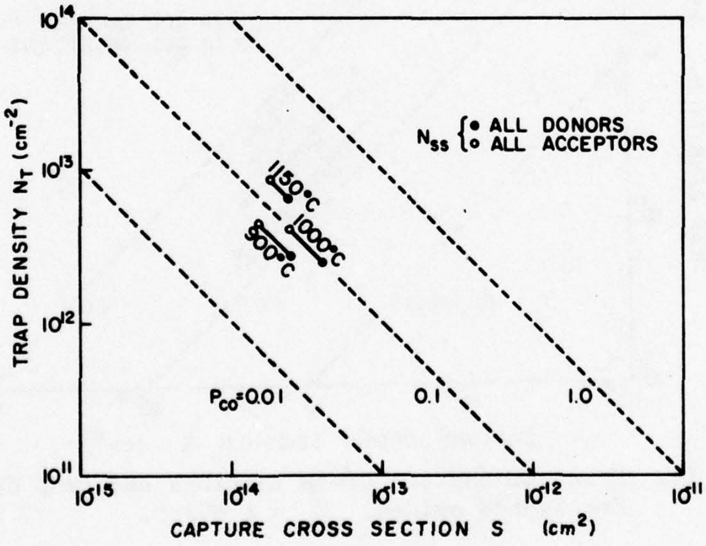

Figure 12. Measured capture cross sections and trap densities for unannealed dry oxides. E_o = 1 MV/cm.

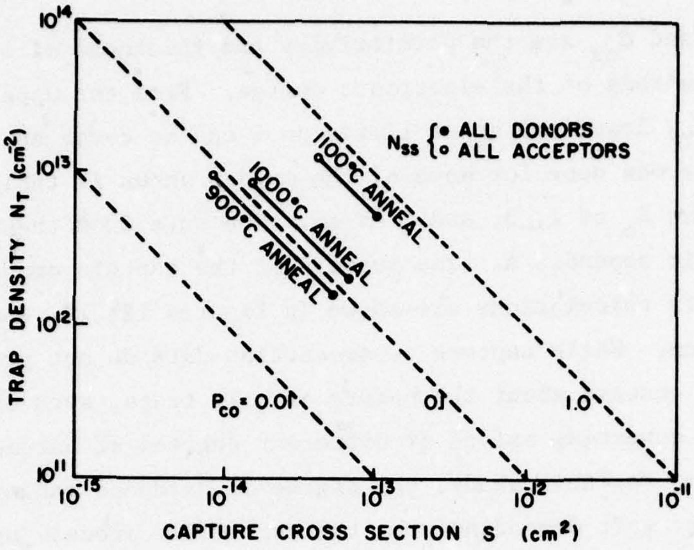

Figure 13. Measured capture cross sections and trap densities for pyrogenic steam oxides. E_o = 1 MV/cm.

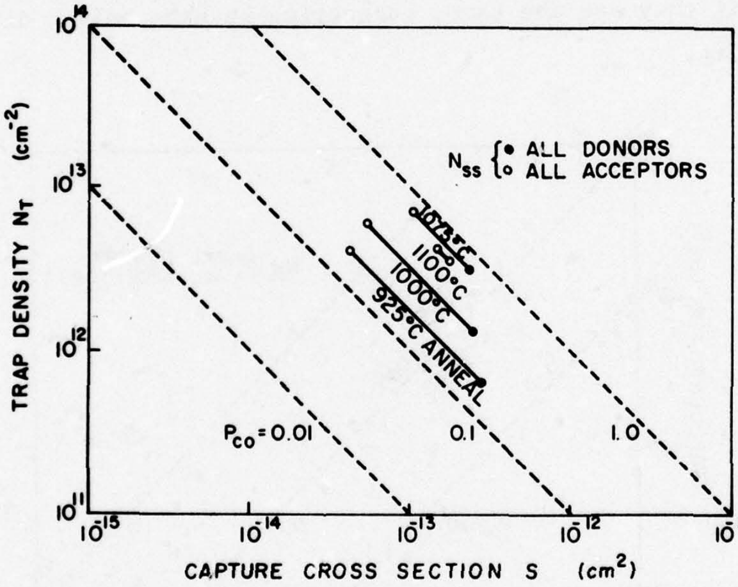

Figure 14. Measured capture cross sections and trap densities for hybrid oxides. E_o = 1 MV/cm.

For the unannealed dry oxides shown in figure 12, it can be seen that the spread in N_T is relatively small, indicating not too many interface states. The initial probability of capture is $\underset{\sim}{\sim}0.1$ for all three oxidations, even though the high-energy 1-Mrad radiation data in figure 6 show a factor of 5 difference in ΔV_{FB} between 900° and 1000°C hard oxides and the 1150°C soft oxide. In addition the DDCV data shown in appendix A indicate no current reversal and therefore few acceptor interface states. However, the spread in N_T indicates *some* interface states present which would suggest that they are mainly donors. The capture cross section S for these oxides is $\underset{\sim}{\sim}5 \times 10^{-14}$ cm^2.

The pyrogenic steam oxides in figure 13 show a much wider spread in N_T indicating many more interface states than the dry oxides. The DDCV data in the appendix show a current reversal, indicating acceptor interface states present. Since we know nothing about the donors, we *cannot say exactly where on the constant* P_{co} lines the data actually lie. Here the capture cross section for the oxide traps is less certain but appears to lie between 5×10^{-14} and 10^{-13} cm^2 for all the oxides taken as a whole. As figure 7 shows, the ΔV_{FB} for high-energy irradiation of these samples ranges over more than an order of magnitude. The 900°C annealed oxide shows a very acceptable 1.3-V shift in figure 7, but as figure 13 shows, the P_{co} is not much different from the soft 1000°C annealed oxide. The differences in hardness shown in figure 7 are probably due mainly to interface states.

The pyrogenic hybrid oxides shown in figure 14 are somewhat anomalous when compared with the dry and steam oxides of figures 13 and 14. The range of possible capture cross sections for the dry and steam oxides overlap enough that we might conclude that the trap involved in all cases is the same and that only the density of traps and interface states are different between the oxides. With the hybrid oxides, however, it becomes increasingly difficult to stretch this argument. Here it appears that a trap with S $\approx 2 \times 10^{-13}$ cm^2 could explain all the hybrid data. This is four times larger than that assumed for the dry oxides. The significant thing about the hybrid data is that the main difference between the 925°C annealed hard oxide (see fig. 8) and the soft oxides is the density of traps and interface states. The capture cross section ranges for all hybrid oxides overlap completely. Here again, as shown for the hard pyrogenic steam oxide, the hard hybrid oxide has a substantial number of interface states. The data in the appendix show that many of these are acceptors, and they therefore must provide a certain amount of compensation for the trapped holes.

The range of uncertainty in N_T and S is delineated in figures 12, 13, and 14. The uncertainty in P_{co} is not shown here but could be as high as $\pm 50\%$ for the worst case. Even at this extreme it is not possible to reconcile all oxides measured and show them as having only one capture cross section. What is significant, however, is that all the dry oxides and the 900° to 1000°C annealed pyrogenic oxides have traps with about the same cross section. This suggests that hole traps in wet and dry oxides are the same. The differences in hardness measured could then be explained by differences in trap density and interface state density alone. The oxides that do not fit in this category may have some sort of impurity-related trap in addition to the *intrinsic* trap of the hard oxides. The hybrid oxides were in fact grown in an ambient of 3% HCl which may very well change the structure of the oxide as well as the trap capture cross section.

The capture cross sections of these hole traps were measured with an oxide field E_o of 1 MV/cm (which is the normal bias field) and E_o = 5 MV/cm (which is the field used for current enhancement). Much to our surprise, the capture cross section was found to be field-dependent so that $S \propto E_o^{-1}$. This is shown in figure 15 for the 1000°C dry oxide (unannealed). We have actually shown P_{co}, the initial probability of capture here, but, as shown in figure 16, ΔV_{FBF} is field-independent, so it is actually S which is field-dependent in P_{co}. The

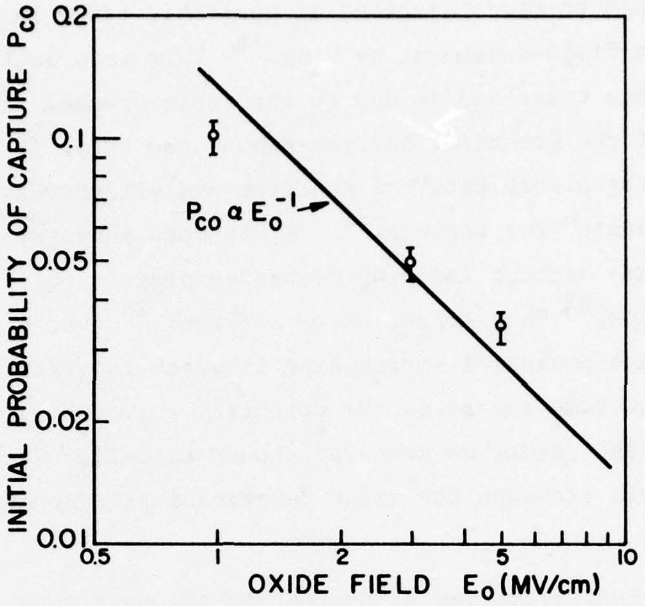

Figure 15. Field dependence of initial probability of capture for unannealed 1000°C dry oxide.

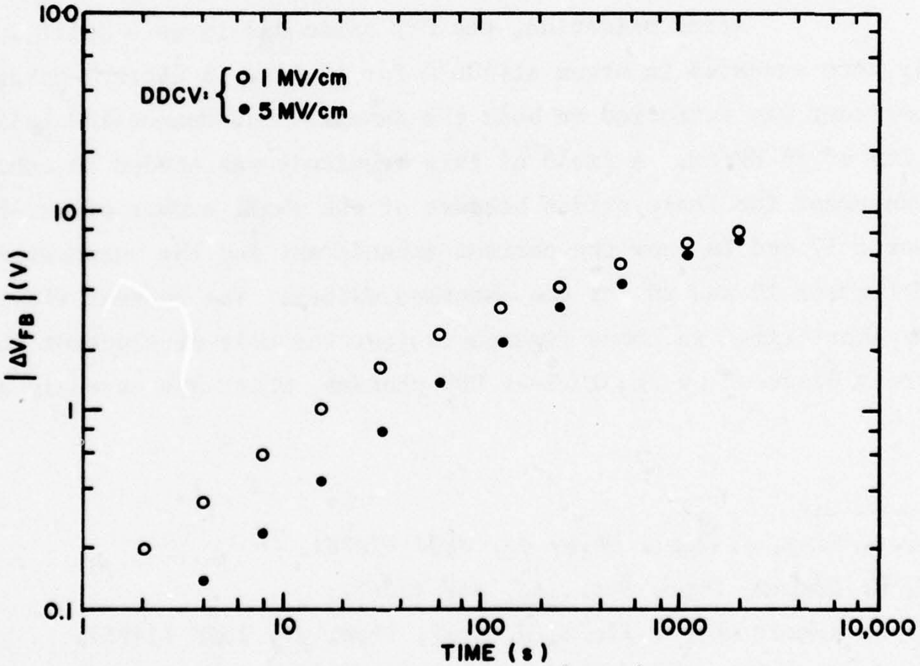

Figure 16. Field dependence of $|\Delta V_{FB}|$ vs t data for unannealed 1000°C dry oxide.

electron capture cross sections of coulombic traps in SiO_2 have been shown to be field-dependent by Ning.[21] This is a well known phenomenon for coulombic traps and is due to the Poole-Frenkel effect or field lowering of the potential barrier around the trap.[22] This decreases the "sticking probability" of the trap and effectively decreases the "critical orbit" for capture.[21] It has been shown by Arnett and Klein that the same barrier lowering mechanism plays a role in capture by neutral traps.[23] They argue, after Jonscher,[24] that a neutral trap has a short-range potential surrounding it which is affected by the applied field in the same way as is the potential surrounding the coulombic trap. All the oxides we measured showed a similar decrease in S with applied field although the exact functional relationship has not been determined.

4.2 Interpretation of Current-Enhancement Data

4.2.1 Dry Oxides

After oxidation, the dry oxide wafers were split in half; half were annealed in argon at 800°C for 15 min. A current-enhancement experiment was performed on both the annealed and unannealed oxide fields of ±6 MV/cm. A field of this magnitude was needed to achieve enhancement for these oxides because of the small number of oxide traps. Figures 17 and 18 show the current enhancement for the unannealed oxides and figures 19 and 20 for the annealed oxides. The current flowing for very short times in these figures is just the hole or electron photocurrent produced by the 10.2-eV VUV photons, which are strongly absorbed

---

[21] *T. H. Ning, J. Appl. Phys. 47, 3203 (1976).*

[22] *J. G. Simons, Phys. Rev. 155, 657 (1967).*

[23] *P. C. Arnett and N. Klein, J. Appl. Phys. 46, 1400 (1975).*

[24] *A. K. Jonscher, Thin Solid Film 1, 213 (1967).*

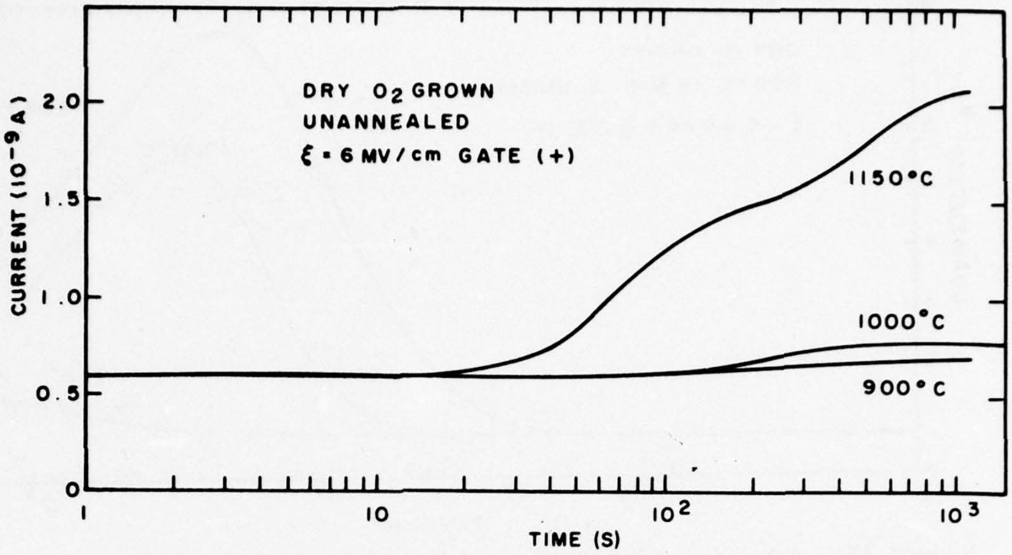

Figure 17. Time dependence of current during VUV irradiation for dry O_2-grown samples with different growth temperatures. Positive gate bias was used to produce an average field of 6 MV/cm in the oxide. The photon energy was 10.2 eV and SiO_2 absorbed photon flux was 4×10^{11} cm^{-2} s^{-1}.

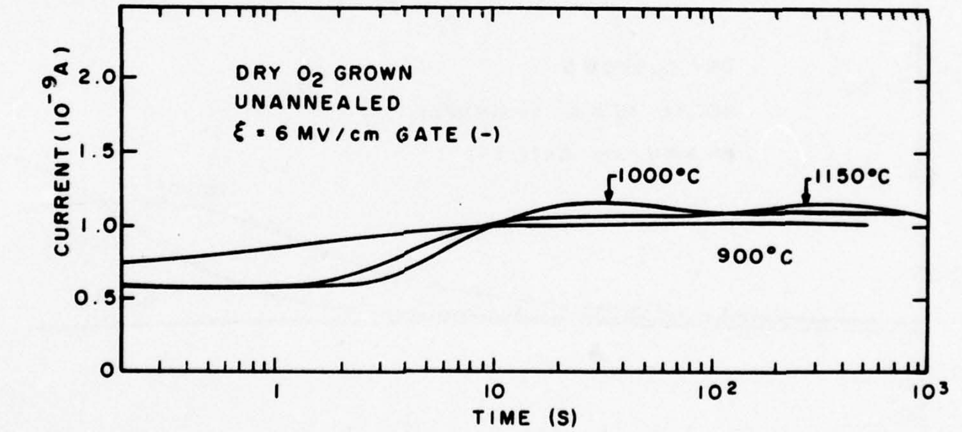

Figure 18. Time dependence of current during VUV irradiation for dry O_2-grown samples with different growth temperatures. Negative gate bias was used. Other conditions were the same as in figure 17.

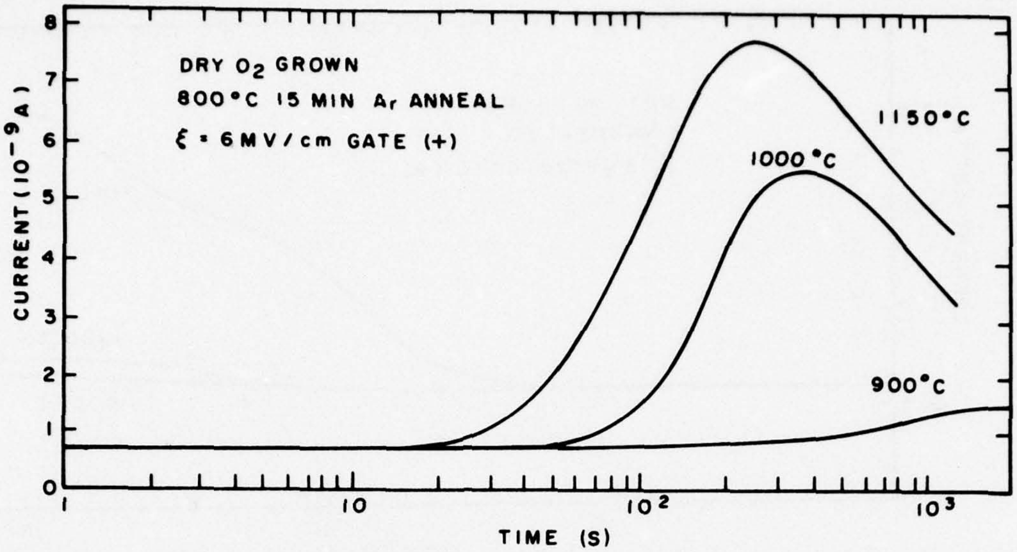

Figure 19. Time dependence of current during VUV irradiation for dry O_2-grown samples which were annealed in argon at 800°C for 15 min. Positive gate bias was used to produce an average oxide field of 6 MV/cm. The photon energy was 10.2 eV and the SiO_2 absorbed photon flux was 4×10^{11} cm^{-2} s^{-1}.

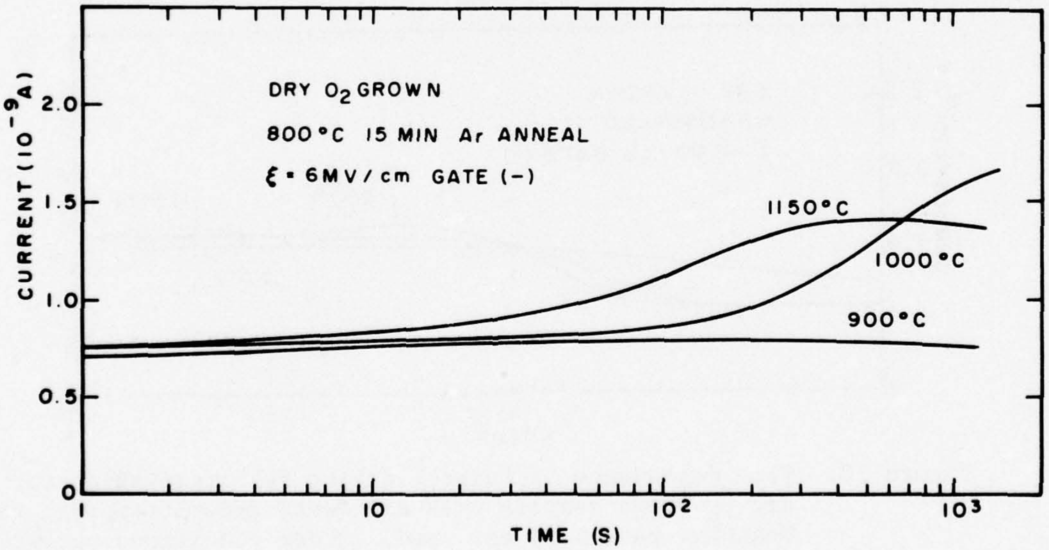

Figure 20. Time dependence of current during VUV irradiation for dry O_2-grown samples which were annealed in argon at 800°C for 15 min. Negative gate bias was used. Other conditions are the same as in figure 19.

in the SiO_2 near the gate electrode. When sufficient space charge accumulates to raise the interface field close to 7 MV/cm, the current increases. The curves in figure 17 show the time dependence of total oxide current for samples with three different growth temperatures. It is apparent from these results that the smallest number of traps is obtained for the lowest growth temperature, 900°C, and the number increases with temperature. The curves in figure 18 depict the current-time characteristics of the unannealed samples under negative gate bias. In this case, holes generated in the shallow absorbing region near the gate are swept out to the gate. Some, however, are trapped in this region, and the accumulating space charge enhances the field at the gate until the current is enhanced by electron tunneling from the gate into the oxide. This experiment provides us with a method of estimating and comparing the number of hole traps effective in enhancing the field at the gate. A surprising fact is that for both the 900° and 1000°C samples the current enhancement is actually larger under negative gate bias than with positive bias. One might be tempted to suggest that in these samples the hole trapping is distributed throughout the oxide with the centroid lying somewhat closer to the gate for the 900° and 1000°C samples. However, that this is definitely not the case is readily proven. First, the trapping in the negative bias case must be almost entirely within 200 Å of the gate electrode because the absorption depth of the 10.2-eV light is only about 100 Å. Second, the capacitance-voltage flatband shifts for negative bias are seven to eight times smaller than for positive bias, as illustrated in figure 21, so we must conclude that the charge is very near the gate electrode following negative bias irradiation.

Charge trapped near the gate will have little effect on the current enhancement and flatband shift under positive bias, and charge is mostly near the Si-SiO_2 interface following positive bias irradiation. Using these facts, we can estimate the location of charge trapped near the gate following negative bias irradiation. The results of

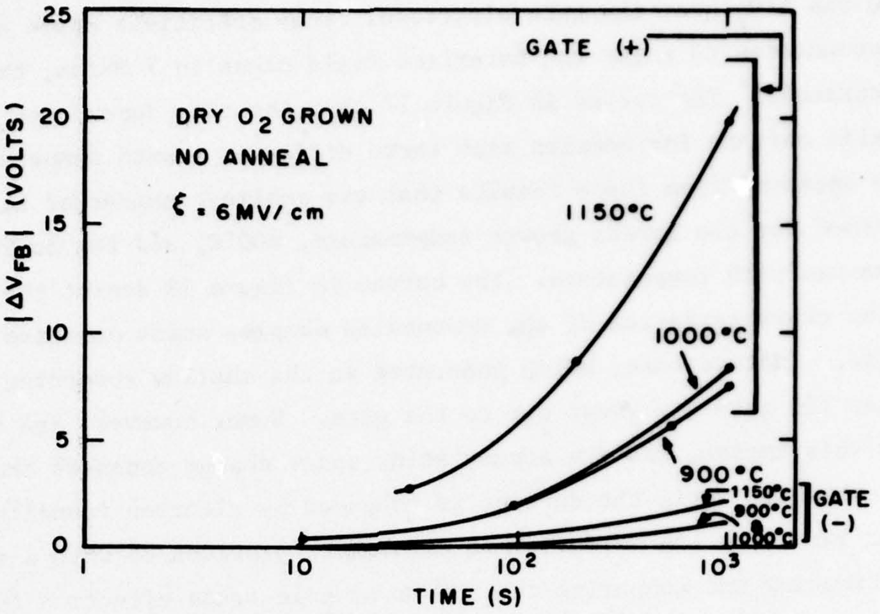

Figure 21. Flatband shift vs time during irradiation with positive and negative bias for unannealed dry oxides.

figures 17 and 18 indicate that for the 900° and 1000°C samples, comparable amounts of charge are trapped near the silicon and aluminum. Since the $|\Delta V_{FB}|$ for the two cases differs by a factor of ∿7, the charge centroid for the negative bias case must be ∿7 times closer to the gate than for the positive bias case. This places the centroid within about 100 Å of the Al-SiO_2 interface. The above argument assumes that the trapped charge is as effective in producing current enhancement as it is in producing flatband shift. This is not true when charge is trapped extremely close to the interface (within ∿30 Å).[25]

---

[25] *R. J. Powell, "Radiation and Charge Injection in Al_2O_3 Using New Techniques," Final Report No. AFGL-TR-76-0017 for Air Force Geophysics Laboratory, January 1976.*

Presented in figures 19 and 20 are curves which summarize the experimental results for VUV current enhancement experiments on the set of samples which was annealed in argon following oxidation. Focusing on figure 19, we first observe the greatly increased current enhancement compared with the unannealed samples in figure 17 (note scale differences between these figures). This result indicates that the argon anneal has markedly increased the number of oxide traps which are effective in producing current enhancement and flatband shifts. This statement is borne out by the flatband shift data shown in figure 22. The shifts here are in every case significantly larger than those of the unannealed oxides (fig. 21). The second observation is that the current begins to decrease for the 1000° and 1150°C oxides at about 250 to 300 s. As explained in section 2.3, this is due to a large increase in acceptor interface states. (Note that only acceptors are charged in positive bias current enhancement.)

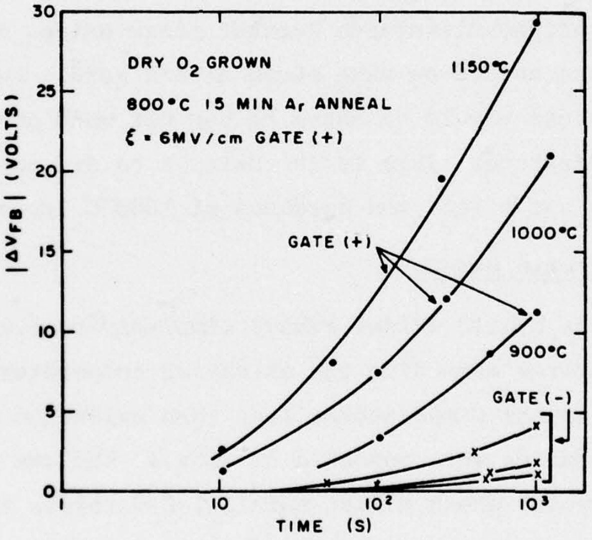

Figure 22. Flatband shift vs time during VUV irradiation with positive and negative gate bias for argon-annealed oxides.

A comparison of figures 20 and 18 shows that the trapping near the gate electrode has not been significantly increased by the argon anneal. These results suggest that the anneal does not appreciably change the basic trap structure of the oxide bulk and near the gate electrode, but does modify it markedly near the $Si-SiO_2$ interface.

4.2.2 Pyrogenic Steam Oxides

In addition to the 900°, 1000°, and 1100°C annealed steam oxides, oxides were also annealed at 850°, 950°, and 1050°C for current-enhancement measurements. Figure 23 shows these results. It is interesting to note here that the minimum current enhancement occurs at 1000°C and the minimum flatband shift occurs at 900°C for high energy irradiation (see fig. 7) and VUV irradiation up to 500 s (fig. 24). It may be that acceptor interface states compensate the trapped holes for current enhancement even before the current starts rising. For hard oxides such as these, a higher applied field is needed to see the effects of hole traps first.

One important difference between steam oxides and dry oxides is that anneals are needed to make steam oxides hard. Furthermore, the anneal temperature should be equal to but not much greater than the oxidation temperature. This is in contrast to dry oxides where anneals below 800°C do not affect the hardness of 1000°C dry oxides at all.

4.2.3 Hybrid Oxides

The hybrid oxides behave similarly to steam oxides for anneal temperatures exceeding the oxidation temperature. (We do not have data for anneal temperatures less than oxidation temperatures since all the oxides were annealed *in situ*.) The one exception is the 1150°C anneal which shows almost parallel C-V shifts indicating very little interface state generation. This is supported by the DDCV and HFCV shifts as shown in figure 25. All the other anneals show acceptor interface state generation as reflected in the reversal of the DDCV ΔV_{FB}. Figure 26 shows the current-enhancement characteristic for these oxides, and figure 27 shows the ΔV_{FB} vs t data.

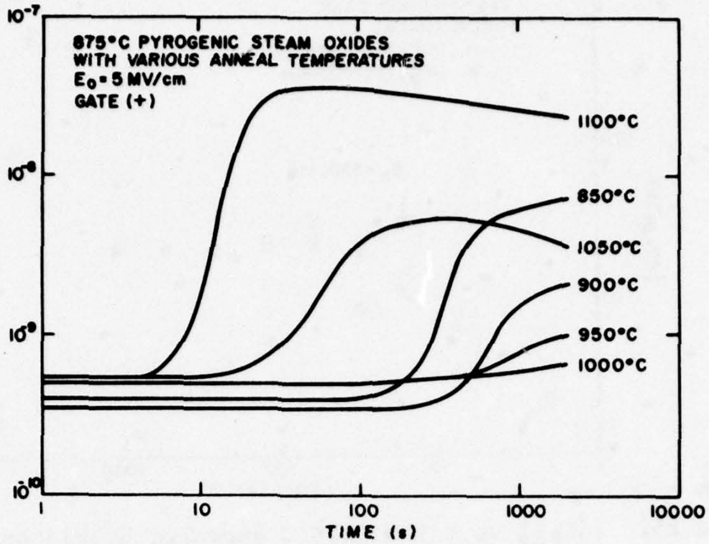

Figure 23. Time dependence of current during irradiation for pyrogenic steam oxides which were annealed at the temperatures shown. Positive gate bias of 5 MV/cm was used. Other conditions were the same as in figure 17.

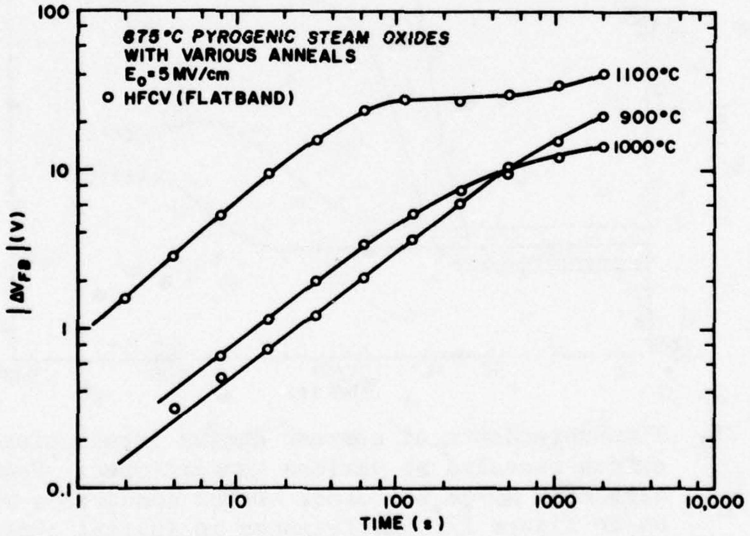

Figure 24. $|\Delta V_{FB}|$ vs t for various anneals of pyrogenic steam oxide. Positive gate bias of 5 MV/cm was used.

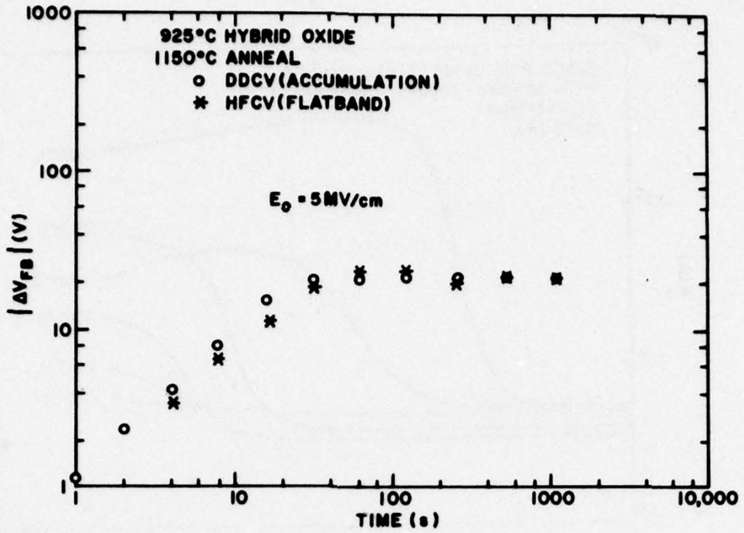

Figure 25. $|\Delta V_{FB}|$ vs t for 1150°C annealed hybrid oxide illustrating little interface state generation.

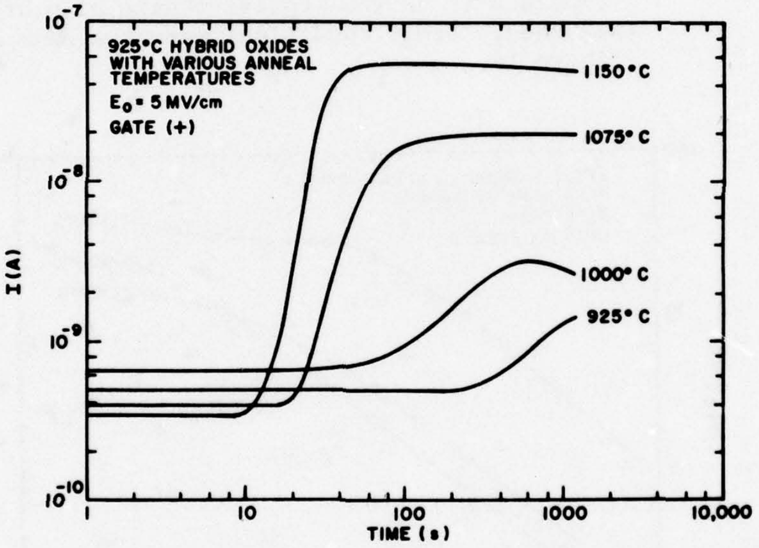

Figure 26. Time dependence of current during irradiation for hybrid oxides annealed at various temperatures. Positive gate bias of 5 MV/cm was used. Other conditions were the same as in figure 17. Differences in initial photocurrent due to varying thickness of semitransparent Al gate.

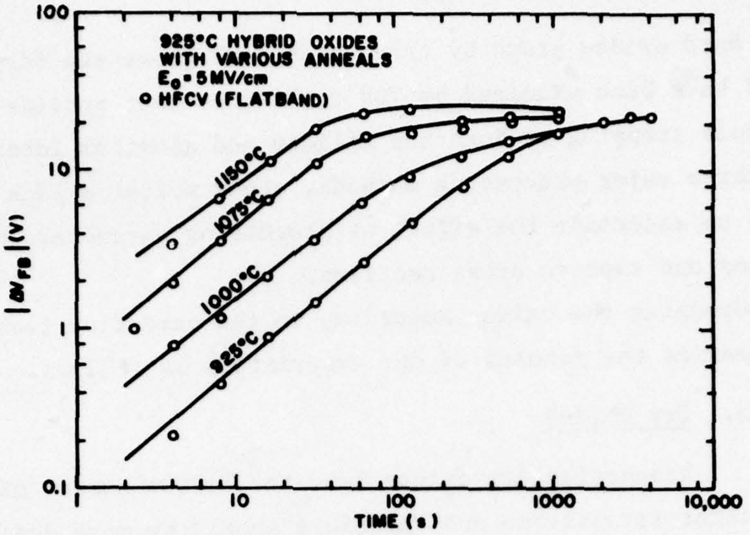

Figure 27. $|\Delta V_{FB}|$ vs t data for hybrid oxides annealed at various temperatures. Positive gate bias of 5 MV/cm was used.

5. SUMMARY AND CONCLUSION

Hard oxides grown by three different processes (dry, wet, and hybrid) have been examined by VUV techniques that provide information about hole trapping at both the silicon and aluminum interface. Within these three major processing methods, other softer oxides were also studied to ascertain the effect of processing parameters on hole-trap densities and capture cross sections.

Grouping the oxides according to the oxidation technique, we can summarize the results of our experiments as follows.

5.1 Dry Oxides

Unannealed dry oxides have the lowest number of interface states after irradiation and therefore should be more desirable for radiation applications where parameters such as switching speed are important. As a group these oxides are dominated by a hole trap with $S \simeq 5 \times 10^{-14}$ cm^2 at 1 MV/cm. The DDCV measurements show no reversal in the ΔV_{FB} vs t data so that the few interface states seen after irradiation are probably donors.

Current-enhancement measurements were made on both annealed and unannealed oxides under positive and negative bias. The unannealed oxides show no enhancement reversal for any of the growth temperatures indicating few acceptor interface states. The 900° and 1000°C oxides are very hard with little current enhancement even at $E_o = 6$ MV/cm. The enhancement under negative bias is actually larger than under positive bias for the 900° and 1000°C oxide which shows that more charge is trapped at the aluminum interface than at the silicon interface for these samples.

Annealing these oxides in argon substantially increases not only the number of hole traps near the silicon interface but also the number of acceptor interface states. The density of the hole traps near the aluminum interface is not affected much by the argon anneal.

5.2 Steam Oxide

Pyrogenic steam oxides have many more interface states than dry oxides even in hard samples. Many or all of these interface states are acceptors. As a group these oxides show $S \simeq 5 \times 10^{-14} - 10^{-13}$ for $E_o = 1$ MV/cm. The hardness of these oxides for high-energy irradiation ranges over an order of magnitude in ΔV_{FB} depending upon anneal temperature. Since all capture cross sections appear to be the same, the wide variation in ΔV_{FB} must be due to wide differences in hole trap and/or interface state densities. Current enhancement measurements show a very strong dependence on anneal temperature with 1000°C having the least enhancement and 850° and 1100°C the most. It is believed that the 900°C annealed oxide has the least number of hole traps and that the 1000°C oxide has less enhancement because of more acceptor interface states. The optimum anneal temperature for steam oxides is equal to or not much greater than the oxidation temperature.

5.3 Hybrid Oxides

In contrast to the other two processes, the hybrid oxides show $S \approx 2 \times 10^{-13}$ cm^2 (at $E_o = 1$ MV/cm) up to 4 times larger than the wet or dry oxide capture cross sections. This is the only group of oxides grown with HCl present during oxidation. It is suspected that the HCl modifies the SiO_2 properties to the extent that the capture cross section is different. More than the other oxides the capture cross sections for the hybrid oxides overlap within the group. The main differences appear to be the hole trap and interface state density (of which many are acceptors).

The current-enhancement data for the hybrid oxides is similar to the wet oxide data. The enhancement increases with anneal temperature and has a minimum at the oxidation temperature. One anomaly among all the oxides is the 1150°C annealed hybrid oxide. It has a very large flatband voltage shift and current enhancement but very few interface states. All other hybrid oxides show substantial acceptor interface-state generation.

If we make the assumption that different hole traps have substantially different capture cross sections, then the wet and dry oxide data support the conclusion that the same trap is responsible for radiation charging in both oxides. This is somewhat surprising in view of the fact that the oxides are grown by completely different processes. However, it may be that the anneal of steam oxides in an inert ambient restructures the Si-SiO_2 interfacial region to be more like dry SiO_2.

The field dependence of the capture cross section was explained in section 4 as resulting from Poole-Frenkel type lowering of the short range potential barrier surrounding a neutral trap. This could have favorable implications for radiation hardening if devices are not irradiated to saturation. If MOS transistors are fabricated with thin oxides, then not only will the oxide field be larger for a given supply voltage, but the thickness dependence of ΔV_{FB} will make the device much harder.[26,27]

Because of the various limitations of the measurement technique described in section 3 it is not possible to measure S and N_T with any greater accuracy using this method. Ning has shown how these parameters can be measured more accurately if one can measure both the injected charge and the flatband shift to a high degree of accuracy.[21] Because of possible charge detrapping with changes in bias, it is not possible to measure ΔV_{FB} more accurately using MOS capacitors. Ning has used MOS transistors to measure threshold-voltage shifts very accurately, presumably because the oxide field is unchanged throughout the measurement.[21] Unfortunately his technique relies on injected

---

[26] *G. F. Derbenwick and B. L. Gregory, IEEE Trans. Nucl. Sci.* NS-22, *2151 (1975).*

[27] *G. W. Hughes, R. J. Powell, and M. H. Woods, Appl. Phys. Lett.* 29, *377 (1976).*

charge from the silicon interface as the probe. This places a limitation on the maximum trapping efficiency that can be measured ($P_{co} \leq 0.1$). With VUV hole and electron excitation at the gate interface, this limitation is overcome since all charge arriving at the Si-SiO_2 interface is measured as a displacement current in the external circuit whether it is trapped or not. Using Ning's approach for measuring threshold-voltage shifts and exciting holes (or electrons) with 10.2-eV VUV photons, we should be able to measure S and N_T over a much wider range of cross sections and with much more accuracy than has been demonstrated at this time. This holds true for hole and electron capture cross sections.

REFERENCES

1. J. R. Srour, S. Othmer, O. L. Curtis, Jr., and K. Y. Chiu, IEEE Trans. Nucl. Sci. NS-23, 1513 (1976).
2. F. B. McLean, H. E. Boesch, Jr., and J. M. McGarrity, IEEE Trans. Nucl. Sci. NS-23, 1506 (1976) and H. E. Boesch, Jr., F. B. McLean, J. M. McGarrity, and G. A. Ausman, Jr., IEEE Trans. Nucl. Sci. NS-22, 2163 (1975).
3. R. C. Hughes, Bull. Am. Phys. Soc. 21, 404 (1976).
4. T. H. DiStephano and D. E. Eastman, Sol. State Comm. 9, 2259 (1971).
5. G. H. Sigel, Jr., E. J. Friebele, R. J. Ginther, and D. L. Griscom, IEEE Trans. Nucl. Sci. NS-21, 56 (1974).
6. C. T. Sah, IEEE Trans. Nucl. Sci. NS-23, 1563 (1976).
7. B. L. Gregory, IEEE Trans. Nucl. Sci. NS-22, 2295 (1975).
8. G. W. Hughes and R. J. Powell, IEEE Trans. Nucl. Sci. NS-23, 1569 (1976).
9. G. W. Hughes, "Radiation and Charge Transport in SiO_2," Final Report prepared under Contract N00014-74-C-0185 for Office of Naval Research, July 1977.
10. T. H. Ning and H. N. Yu, J. Appl. Phys. 45, 5373 (1974).
11. J. M. Aitken, D. J. DiMaria, and D. R. Young, IEEE Trans. Nucl. Sci. NS-23, 1526 (1976).
12. R. J. Powell, J. Appl. Phys. 46, 4557 (1975).
13. G. W. Hughes, J. Appl. Phys. 48, 5357 (1977).
14. R. J. Powell and G. W. Hughes, "Radiation and Charge Transport in SiO_2," Annual Report prepared under Contract N00014-74-C-0185 for Office of Naval Research, January 1975.
15. F. P. Heiman and G. Warfield, IEEE Trans. Electron. Devices ED-12, 167 (1965).
16. L. Katz and A. S. Penfold, Rev. of Modern Physics 24, 28 (1952).
17. J. R. Srour, O. L. Curtis, and K. Y. Chiu, IEEE Trans. Nucl. Sci. NS-21, 73 (1974). For analysis of data in preceding reference, see G. A. Ausman, Jr. and F. B. McLean, Appl. Phys. Letters 26, 173 (1975).
18. G. W. Hughes, R. M. Hughes, and R. M. White, IEEE Trans. Electron. Devices ED-22, 945 (1975).
19. J. G. Simmons and L. S. Wei, Solid State Electronics 16, 53 (1973).

20. S. M. Sze, *Physics of Semiconductor Devices* (John Wiley & Sons, New York, 1969), p. 455.

21. T. H. Ning, J. Appl. Phys. 47, 3203 (1976).

22. J. G. Simmons, Phys. Rev. 155, 657 (1967).

23. P. C. Arnett and N. Klein, J. Appl. Phys. 46, 1400 (1975).

24. A. K. Jonscher, Thin Solid Film 1, 213 (1967).

25. R. J. Powell, "Radiation and Charge Injection in Al_2O_3 using New Techniques" Final Report No. AFGL-TR-76-0017 for Air Force Geophysics Laboratory, January 1976.

26. G. F. Derbenwick and B. L. Gregory, IEEE Trans. Nucl. Sci. NS-22, 2151 (1975).

27. G. W. Hughes, R. J. Powell, and M. H. Woods, Appl. Phys. Lett. 29, 377 (1976).

APPENDIX

APPENDIX A. CALCULATION OF CAPTURE CROSS SECTION AND TRAP DENSITY

To calculate the capture cross section S and the trap density N_T for the various oxides, two different sets of data are needed. The initial flatband shift as a function of time is used to determine the product $N_T S$ through the use of equation (21) from the main body of this report. This assumes ΔV_{FB} is initially linear with t. This is true for most oxides, but there is one exception: the 925°C annealed hybrid oxide (see fig. A-1). Equation (21) was used for this case anyway, as a first approximation to $N_T S$. Figures A-1 through A-3 contain these data for all oxides measured at E_o = 1 MV/cm.

The final ΔV_{FB} was determined from the DDCV and HFCV data as explained in section 3 of this report. ΔV_{FBF} is not a strong function of applied field as long as E_o is large enough to inhibit geminate recombination at the gate (see fig. 16 in the main body of the report). These measurements were only taken at E_o = 5 MV/cm. Fields of this magnitude as necessary to eliminate any reduction in hole generation rate due to charge build-up at the gate.[A-1] Figures 11 and 25 and figures A-4 through A-11 contain these data for all oxides measured at E_o = 5 MV/cm.

[A-1] *R. J. Powell, J. Appl. Phys.* 46, *4557 (1975).*

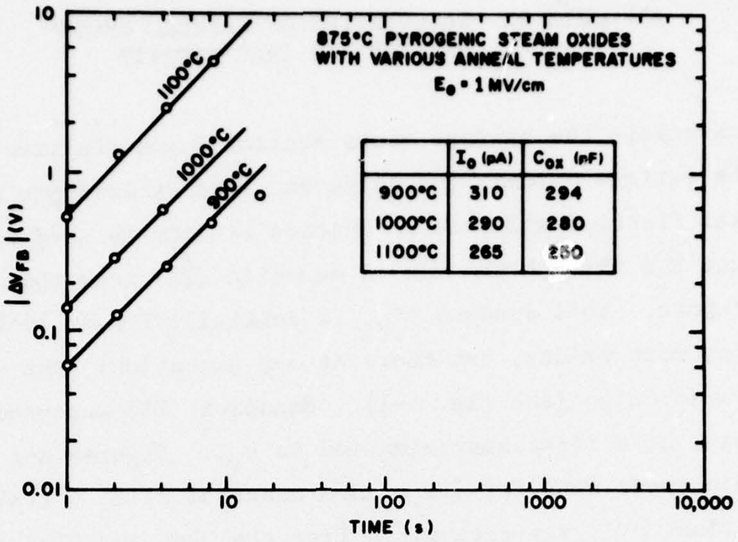

	I_0 (pA)	C_{ox} (pF)
900°C	310	294
1000°C	290	280
1100°C	265	250

Figure A-1. $|\Delta V_{FB}|$ vs time "early" data for pyrogenic steam oxides annealed at various temperatures.

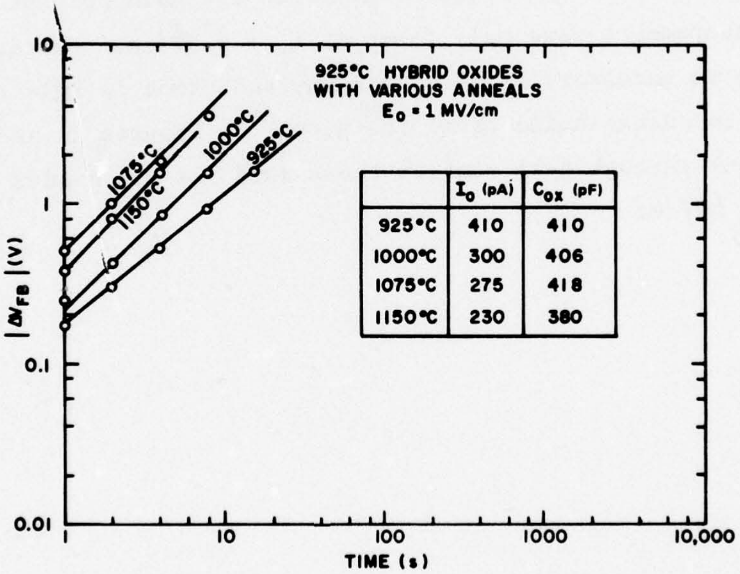

	I_0 (pA)	C_{ox} (pF)
925°C	410	410
1000°C	300	406
1075°C	275	418
1150°C	230	380

Figure A-2. $|\Delta V_{FB}|$ vs time "early" data for hybrid oxides annealed at various temperatures.

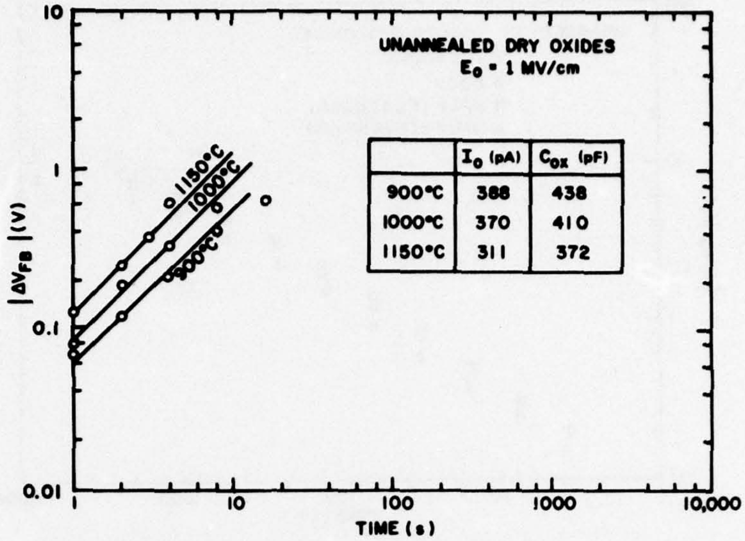

Figure A-3. $|\Delta V_{FB}|$ vs time "early" data for unannealed dry oxides grown at various temperatures.

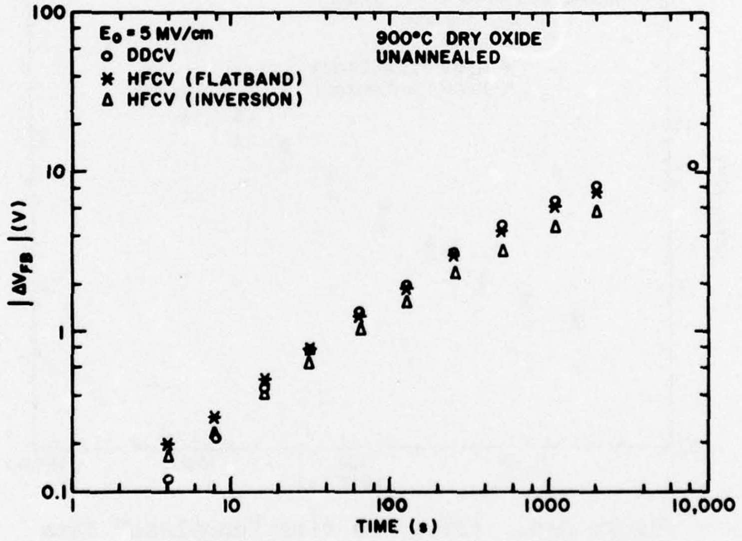

Figure A-4. $|\Delta V_{FB}|$ vs time "complete" data for 900°C dry oxides.

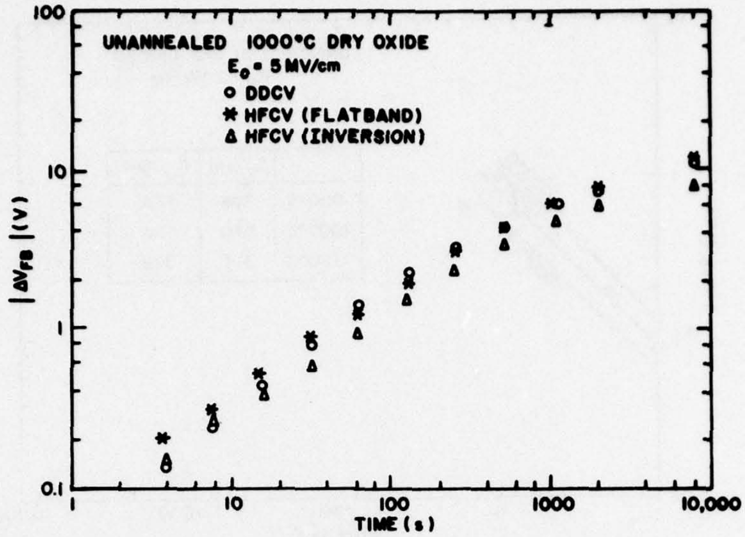

Figure A-5. $|\Delta V_{FB}|$ vs time "complete" data for 1000°C dry oxides.

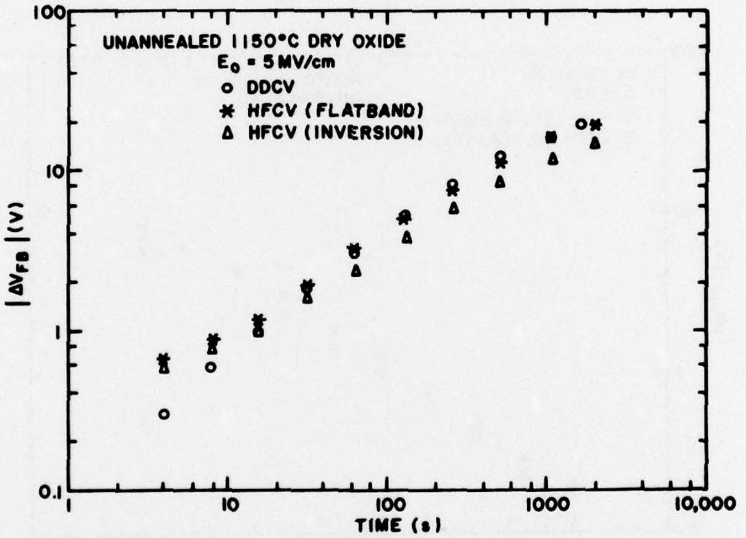

Figure A-6. $|\Delta V_{FB}|$ vs time "complete" data for 1150°C dry oxides.

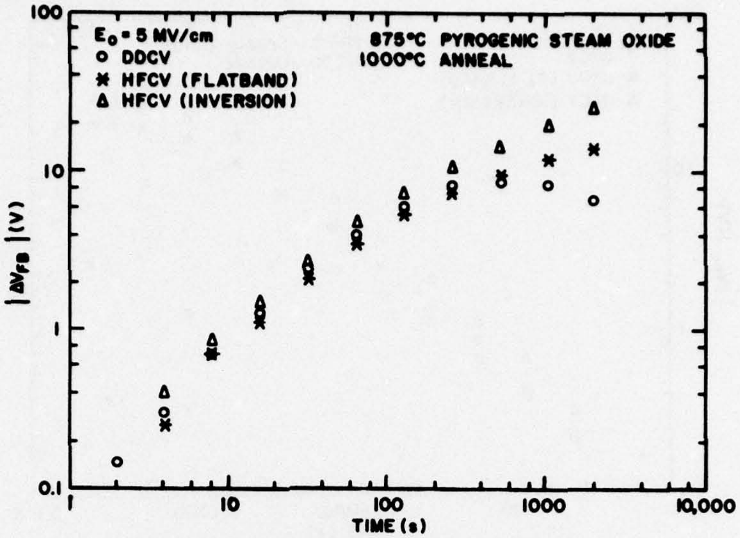

Figure A-7. $|\Delta V_{FB}|$ vs time "complete" data for 1000°C annealed pyrogenic steam oxide.

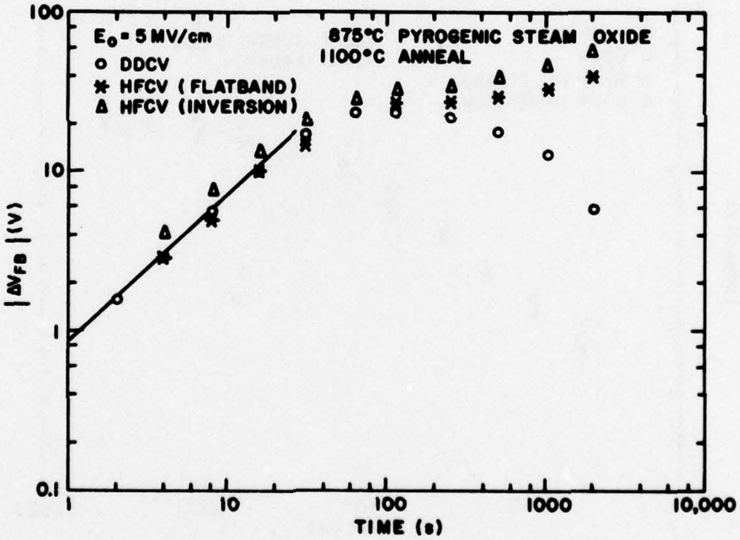

Figure A-8. $|\Delta V_{FB}|$ vs time "complete" data for 1100°C annealed pyrogenic steam oxide.

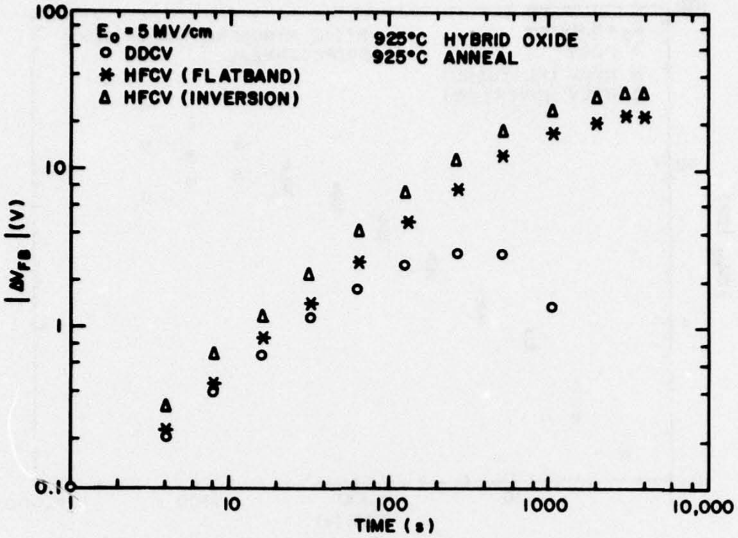

Figure A-9. $|\Delta V_{FB}|$ vs time "complete" data for 925°C annealed hybrid oxide.

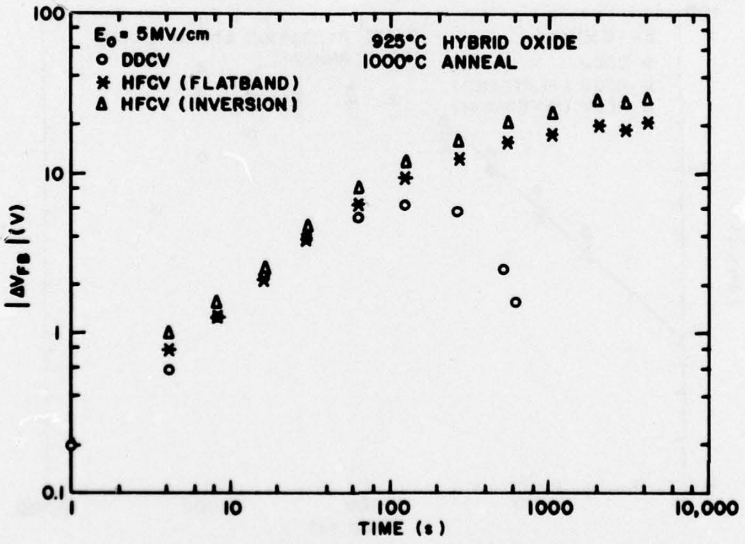

Figure A-10. $|\Delta V_{FB}|$ vs time "complete" data for 1000°C annealed hybrid oxide.

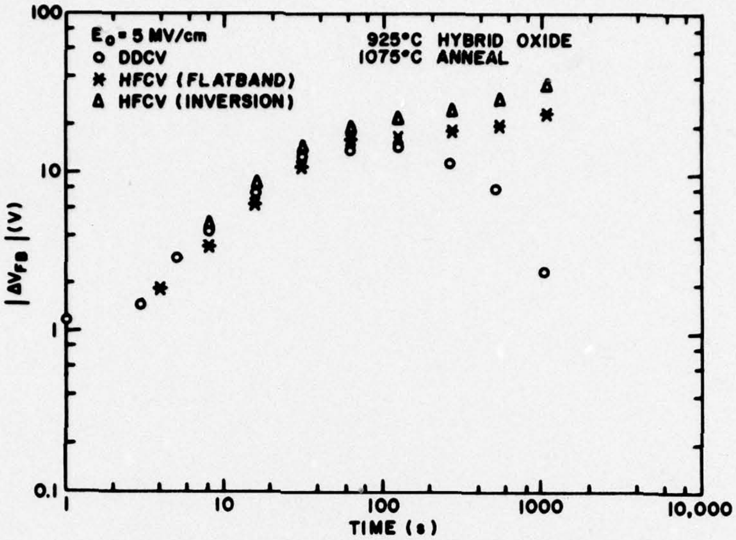

Figure A-11. $|\Delta V_{FB}|$ vs time "complete" data for 1075°C annealed hybrid oxide.

DISTRIBUTION LIST

Director
Defense Communications Agency
Washington, DC 20305
Attn: Code 930, M.I. Burgett

Defense Documentation Center
Cameron Station
Alexandria, VA 22314
(12)

Director
Defense Intelligency Agency
Washington, DC 20301
Attn: DS-4A2

Director
Defense Nuclear Agency
Washington, DC 20305
Attn: DDST

Director
Defense Nuclear Agency
Washington, DC 20305
Attn: TITL Tech Library
(3)

Director
Defense Nuclear Agency
Washington, DC 20305
A-tn: RAEV

Director
Defense Nuclear Agency
Washington, DC 20305
Attn: RATN

Director
Defense Nuclear Agency
Washington, DC 20305
Attn: STVL

Dir of Defense Rsch & Eng
Department of Defense
Washington, DC 20301
Attn: S&SS (OS)

Commander
Field Command
Defense Nuclear Agency
Kirtland AFB, NM 87115
Attn: FCPR

Director
Interservice Nuclear Weapons Sch
Kirtland AFB, NM 87115
Attn: Document Control

Director
Joint Strat Tgt Planning
Staff JCS - JLTW-2
Offutt AFB
Omaha, NB 68113

Livermore Div Fld Command DNA
Livermore Laboratory
P.O. Box 808
Livermore, CA 94550
Attn: FCPRL

Director
National Security Agency
Ft. George G. Meade, MD 20755
Attn: O.O. Van Gunten, R-425

Director
National Security Agency
Ft. George G. Meade, MD 20755
Attn: TDL

Project Manager
Army Tactical Data Systems
U.S. Army Electronics Command
Fort Monmouth, NJ 07703
Attn: D.B. Huewe

Project Manager
Army Tactical Data Systems
U.S. Army Electronics Command
Fort Monmouth, NJ 07703
Attn: DRCPN-TDS-SD

Commander
BMD System Command
P.O. Box 1500
Huntsville, AL 35807
Attn: BDMSC-TEN

Commander
Frankford Arsenal
Bridge & Tacony Sts
Philadelphia, PA 19137
Attn: SARFA-FCD

Commander
Harry Diamond Laboratories
2800 Powder Mill Road
Adelphi, MD 20783
Attn: J. Halpin

Commander
Harry Diamond Laboratories
2800 Powder Mill Road
Adelphi, MD 20783
Attn: DRSCO-TI, Tech Lib
(3)

Commander
Harry Diamond Laboratories
2800 Powder Mill Road
Adelphi, MD 20783
Attn: DRXDO-RCC

Commander
Harry Diamond Laboratories
2800 Powder Mill Road
Adelphi, MD 20783
Attn: DRXDO-NP

Commander
Harry Diamond Laboratories
2800 Powder Mill Road
Adelphi, MD 20783
Attn: DRXDO-RCC

Commander
Harry Diamond Laboratories
2800 Powder Mill Road
Adelphi, MD 20783
Attn: J. McGarrity

Commander
Harry Diamond Laboratories
2800 Powder Mill Road
Adelphi, MD 20783
Attn: DRXDO-RC

Commander
Harry Diamond Laboratories
2800 Powder Mill Road
Adelphi, MD 20783
Attn: DRXDO-EM

Commander
Harry Diamond Laboratories
2800 Powder Mill Road
Adelphi, MD 20783
Attn: DRXDO-RBH

Commander
Harry Diamond Laboratories
2800 Powder Mill Road
Adelphi, MD 20783
Attn: DRXDO-AS

Commander
Harry Diamond Laboratories
2800 Powder Mill Road
Adelphi, MD 20783
Attn: Chairman, Editorial Cmte

Commander
Harry Diamond Laboratories
2800 Powder Mill Road
Adelphi, MD 20783
Attn: DRXDO-RBH, F. McLean
(10)

Commander
Harry Diamond Laboratories
2800 Powder Mill Road
Adelphi, MD 20783
Attn: DRXDO-TI, Tech Reports

Commander
Harry Diamond Laboratories
2800 Powder Mill Road
Adelphi, MD 20783
Attn: DRXDO-RD, Q.C. Kaiser

Commander
Picatinny Arsenal
Dover, NJ 07801
Attn: SMUPA-ND-W

Commander
Picatinny Arsenal
Dover, NJ 07801
Attn: SMUPA-ND-N-E

Commander
Picatinny Arsenal
Dover, NJ 07801
Attn: SARPA-ND-C-E

Commander
Picatinny Arsenal
Dover, NJ 07801
Attn: SARPA-FR-F

Commander
Picatinny Arsenal
Dover, NJ 07801
Attn: SARPA-ND-N

Commander
Redstone Scientific Info Ctr
U.S. Army Missile Command
Redstone Arsenal, AL 35809
Attn: Chief, Documents (3)

Secretary of the Army
Washington, DC 20310
Attn: ODUSA-OR

Director
TRASANA
White Sands Missile Range
New Mexico 88002
Attn: ATAA-EAC

Director
U.S. Army Ballistic Research Lbs
Aberdeen Prvng Ground, MD 21005
Attn: DRXBR-AM

Director
U.S. Army Ballistic Research Lbs
Aberdeen Prvng Ground, MD 21005
Attn: DRXBR-X

Director
U.S. Army Ballistic Research Lbs
Aberdeen Prvng Ground, MD 21005
Attn: DRXRD-BVL

Chief
U.S. Army Communications
Sys Agency
Fort Monmouth, NJ 07703
Attn: SCCM-AD-SV, Library

Commander
U.S. Army Electronics Command
Fort Monmouth, NJ 07703
Attn: DRSEL-TL-MD

Commander
U.S. Army Electronics Command
Fort Monmouth, NJ 07703
Attn: DRSEL-TL-EN

Commander
U.S. Army Electronics Command
Fort Monmouth, NJ 07703
Attn: DRSEL-CT-HDK

Commander
U.S. Army Electronics Command
Fort Monmouth, NJ 07703
Attn: DRSEL-GG-TD

Commander
U.S. Army Electronics Command
Fort Monmouth, NJ 07703
Attn: DRSEL-TL-IR

Commander
U.S. Army Electronics Command
Fort Monmouth, NJ 07703
Attn: DRSEL-TL-ND

Commander
U.S. Army Electronics Command
Fort Monmouth, NJ 07703
Attn: DRSEL-TL-EN

Commander
U.S. Army Electronics Command
Fort Monmouth, NJ 07703
Attn: DRSEL-PL-ENV

Commander-In-Chief
U.S. Army Europe & Seventh Army
APO New York 09403
Attn: ODCSE-E AEAGE-PI

Commander
U.S. Army Missile Command
Redstone Arsenal, AL 35809
Attn: DRSMI-RGD

Commander
U.S. Army Missile Command
Redstone Arsenal, AL 35809
Attn: DRCPM-LCEX

Commander
U.S. Army Missile Command
Redstone Arsenal, AL 35809
Attn: DRSMI-RGP

Commander
U.S. Army Missile Command
Redstone Arsenal, AL 35809
Attn: DRSMI-RRR

Commander
U.S. Army Missile Command
Redstone Arsenal, AL 35809
Attn: DRCPM-PE-EA

Commander
U.S. Army Mobility Equip R&D Ctr
Fort Belvoir, VA 22060
Attn: STSFB-MW

Chief
U.S. Army Nuc & Chemical Surety
Bldg 2073, North Area
Ft. Belvoir, VA 22060
Attn: MOSG-ND

Commander
U.S. Army Nuclear Agency
7500 Backlick Rd, Bldg 2073
Springfield, VA 22150
Attn: ATCN-W

Commander
U.S. Army Test & Eval Command
Aberdeen Prvng Ground, MD 21005
Attn: DRSTE-EL

Commander
U.S. Army Test & Eval Command
Aberdeen Prvng Ground, MD 21005
Attn: DRSTE-NB

Chief of Naval Research
Navy Department
Arlington, VA 22217
Attn: Code 421

Chief of Naval Research
Navy Department
Arlington, VA 22217
Attn: Code 427

Commander
Naval Electronic Sys Command
Washington, DC 20360
Attn: PME 117-21

Commander
Naval Electronic Sys Command
Washington, DC 20360
Attn: Code 504510

Commander
Naval Electronic Sys Command
Washington, DC 20360
Attn: ELEX 05323

Commanding Officer
Naval Intelligence Support Ctr
4301 Suitland Road, Bldg 5
Washington, DC 20390
Attn: P. Alexander

Director
Naval Research Laboratory
Washington, DC 20375
Attn: Code 6631

Director
Naval Research Laboratory
Washington, DC 20375
Attn: Code 5216

Director
Naval Research Laboratory
Washington, DC 20375
Attn: Code 7701

Director
Naval Research Laboratory
Washington, DC 20375
Attn: Code 6440

Director
Naval Research Laboratory
Washington, DC 20375
Attn: Code 601

Director
Naval Research Laboratory
Washington, DC 20375
Attn: Code 2627

Director
Naval Research Laboratory
Washington, DC 20375
Attn: Code 4004

Commander
Naval Research Laboratory
Washington, DC 20375
Attn: Code 5210

Commander
Naval Sea Systems Command
Navy Department
Washington, DC 20362
Attn: SEA-9931

Commander
Naval Sea Systems Command
Navy Department
Washington, DC 20362
Attn: SEA-9931

Commander
Naval Ship Engineering Ctr
Washington, DC 20362
Attn: Code 6174D2

Officer-In-Charge
Naval Surface Weapons Center
White Oak
Silver Spring, MD 20910
Attn: Code WA52

Officer-In-Charge
Naval Surface Weapons Center
White Oak
Silver Spring, MD 20910
Attn: Code WA50

Officer-In-Charge
Naval Surface Weapons Center
White Oak
Silver Spring, MD 20910
Attn: Code WA501, NNPO

Commander
Naval Surface Weapons Center
Dahlgren Laboratory
Dahlgren, VA 22448
Attn: W.H. Holt

Commander
Naval Weapons Center
China Lake, CA 93555
Attn: Code 533, Tech Lib

Commanding Officer
Naval Weapons Support Center
Crane, IN 47522
Attn: Code 7024

Commanding Officer
Naval Weapons Support Center
Crane, IN 47522
Attn: Code 70242

Commanding Officer
Nuclear Weapons Tng Ctr Pacific
Naval Air Station, North Island
San Diego, CA 92135
Attn: Code 50

Director
Strategic Sys Project Office
Navy Department
Washington, DC 20376
Attn: NSP-2342

AF Geophysics Laboratory, AFSC
Hanscom AFB, MA 01731
Attn: J.E. Cormier

AF Geophysics Laboratory, AFSC
Hanscom AFB, MA 01731
Attn: LQR, E.A. Burke

AF Institute of Technology, AU
Wright-Patterson AFB, OH 45433
Attn: ENP, C.J. Bridgman

AF Materials Laboratory, AFSC
Wright-Patterson AFB, OH 45433
Attn: LTE

AF Weapons Laboratory, AFSC
Kirtland AFB, NM 87117
Attn: ELS

AF Weapons Laboratory, AFSC
Kirtland AFB, NM 87117
Attn: ELA

AF Weapons Laboratory, AFSC
Kirtland AFB, NM 87117
Attn: DES

AF Weapons Laboratory, AFSC
Kirtland AFB, NM 87117
Attn: NTS

AF Weapons Laboratory, AFSC
Kirtland AFB, NM 87117
Attn: ELP

AF Weapons Laboratory, AFSC
Kirtland AFB, NM 87117
Attn: SAB

AFTAC
Patrick AFB, FL 32925
Attn: TAE

AFTAC
Patrick AFB, FL 32925
Attn: TFS

Air Force Avionics Lab, AFSC
Wright-Patterson AFB, OH 45433
Attn: AAT, M. Friar

Air Force Avionics Lab, AFSC
Wright-Patterson AFB, OH 45433
Attn: DH, LTC McKenzie

Air Force Avionics Lab, AFSC
Wright-Patterson AFB, OH 45433
Attn: DHE, H.J. Hennecke

Commander
ASD
Wright-Patterson AFB, OH 45433
Attn: ENACC,R.L. Fish

Headquarters
Electronic Systems Div/YS
Hanscom AFB, MA 01731
Attn: YSEV

Commander
Foreign Technology Div, AFSC
Wright-Patterson AFB, OH 45433
Attn: ETDP

Commander
Rome Air Development Ctr, AFSC
Griffiss AFB, NY 13440
Attn: RBRP

Commander
Rome Air Development Ctr, AFSC
Hanscom AFB, MA 01731
Attn: ETS, R. Dolan

Commander
Rome Air Development Ctr, AFSC
Hanscom AFB, MA 01731
Attn: ET, R. Buchanan

SAMSO
P.O. Box 92960
Worldway Postal Center
Los Angeles, CA 90009
Attn: DYS

SAMSO
P.O. Box 92960
Worldway Postal Center
Los Angeles, CA 90009
Attn: YEE

SAMSO/IN
P.O. Box 92960
Worldway Postal Center
Los Angeles, CA 90009
Attn: IND I J Judy

SAMSO/MN
Norton AFB, CA 92409
Attn: MNNH

SAMSO/MN
Norton AFB, CA 92409
Attn: MNNG

SAMSO/RS
P.O. Box 92960
Worldway Postal Center
Los Angeles, CA 90009
Attn: RSSE

SAMSO/RS
P.O. Box 92960
Worldway Postal Center
Los Angeles, CA 90009
Attn: RSMG

SAMSO/SZ
P.O. Box 92960
Worldway Postal Center
Los Angeles, CA 90009
Attn: SZJ

Commander-In-Chief
Strategic Air Command
Offutt AFB, NB 68113
Attn: NRI-STINFO Library

Commander-In-Chief
Strategic Air Command
Offutt AFB, NB 68113
Attn: XPFS

University of California
Livermore Laboratory
P.O. Box 808
Livermore, CA 94550
Attn: Tech Info Dept L-3

University of California
Livermore Laboratory
P.O. Box 808
Livermore, CA 94550
Attn: R.L. Ott L-531

University of California
Livermore Laboratory
P.O. Box 808
Livermore, CA 94550
Attn: J.E. Keller L-125

University of California
Livermore Laboratory
P.O. Box 808
Livermore, CA 94550
Attn: H. Kruger L-96

University of California
Livermore Labojratory
P.O. Box 808
Livermore, CA 94550
Attn: L. Cleland L-156

University of California
Livermore Laboratory
P.O. Box 808
Livermore, CA 94550
Attn: F. Kovar L-31

University of California
Livermore Laboratory
P.O. Box 808
Livermore, CA 94550
Attn: D. Meeker L-545

Los Alamos Scientific Lab
P.O. Box 1663
Los Alamos, NM 87545
Attn: Doc Con for B.W. Noel

Los Alamos Scientific Lab
P.O. Box 1663
Los Alamos, NM 87545
Attn: Doc Con for J.A. Freed

Los Alamos Scientific Lab
P.O. Box 1663
Los Alamos, NM 87545
Attn: Doc for M.W. Hoffman

Sandia Laboratories
Livermore Laboratory
P.O. Box 969
Livermore, CA 94550
Attn: Doc Con for T.A. Dellin

Control Data Corporation
P.O. Box 0
Minneapolis, MN 55440
Attn: J. Meehan

Cutler-Hammer, Inc
AIL Division
Comac Road
Deer Park, NY 11729
Attn: Central Tech Files

Dikewood Industries, Inc
1009 Bradbury Drive, S.E.
Albuquerque, NM 87106
Attn: L. Wayne Davis

E-Systems, Inc
Greenville Division
P.O. Box 1056
Greenville, TX 75401
Attn: Library 8-50100

Effects Technology, Inc
5383 Hollister Avenue
Santa Barbara, CA 93111
Attn: E.J. Steele

Exp & Math Physics Consultants
P.O. Box 66331
Los Angeles, CA 90066
Attn: T.M. Jordan

Fairchild Camera & Instrument
464 Ellis Street
Mountain View, CA 94040
Attn: Sec Dept for 2-233
D.K. Myers

Fairchild Industries, Inc
Fairchild Technology Center
20301 Century Boulevard
Germantown, MD 20767
Attn: Mgr, Config Data & Stdrds

University of Florida
P.O. Box 284
Gainesville, FL 32601
Attn: P.B. Rambo

University of Florida
P.O. Box 284
Gainesville, FL 32601
Attn: D.P. Kennedy

Ford Aerospace & Comm Corp
3939 Fabian Way
Palo Alto, CA 94303
Attn: S.R. Crawford, MS 531

Ford Aerospace & Comm Corp
3939 Fabian Way
Palo Alto, CA 94303
Attn: D.R. McMorrow, MS G30

Ford Aerospace & Comm Operations
Ford & Jamboree Roads
Newport Beach, CA 92663
Attn: Tech Info Section

Ford Aerospace & Comm Operations
Ford & Jamboree Roads
Newport Beach, CA 92663
Attn: K.C. Attinger

Franklin Institute
20th Street & Parkway
Philadelphia, PA 19103
Attn: R.H. Thompson

General Dynamics Corp
Electronics Div
P.O. Box 2566
Orlando, FL 32802
Attn: D.W. Coleman

General Electric
Valley Forge Space Center
P.O. Box 8555
Philadelphia, PA 19101
Attn: J.C. Peden RM 4230M

General Electric
Valley Forge Space Center
P.O. Box 8555
Philadelphia, PA 19101
Attn: J.L. Andrews

General Electric
Valley Forge Space Center
P.O. Box 8555
Philadelphia, PA 19101
Attn: L.I. Chasen

General Electric
Re-Entry & Environmental Sys Div
P.O. Box 7722
Philadelphia, PA 19101
Attn: R.V. Benedict

General Electric
Re-Entry & Environmental Sys Div
P.O. Box 7722
Philadelphia, PA 19101
Attn: J.W. Palchefsky Jr

General Electric
Ordnance Systems
100 Plastics Avenue
Pittsfield, MA 01201
Attn: J.J. Reidl

General Electric
Tempo-Center for Adv Studies
816 State Street
Santa Barbara, CA 93102
Attn: R.R. Rutherford

General Electric
Tempo-Center for Adv Studies
816 State Street
Santa Barbara, CA 93102
Attn: DASIAC

General Electric
Tempo-Center for Adv Studies
816 State Street
Santa Barbara, CA 93102
Attn: M. Espig

General Electric
Aircraft Eng Bus Group
Evendale Plant Int Hwy 75S
Cincinnati, OH 45215
Attn: J.A. Ellerhorst E2

General Electric
Aerospace Electronics Systems
French Road
Utica, NY 13503
Attn: W.J. Patterson Drop 233

General Electric
P.O. Box 5000
Binghamton, NY 13902
Attn: D.W. Pepin Drop 160

General Electric
Attn: DASIAC
c/o Defense Nuclear Agency
Washington, DC 20305
Attn: W. Alfonte

General Research Corp
P.O. Box 3587
Santa Barbara, CA 93105
Attn: R.D. Hill

Georgia Institute of Tech
Georgia Tech Research Inst
Atlanta, GA 30332
Attn: R. Curry

Grumman Aerospace Corp
South Oyster Bay Road
Bethpage, NY 11714
Attn: J. Rogers Dept 533

GTE Sylvania, Inc
Electronics Systems Grp
77 A Street
Needham, MA 02194
Attn: L.L. Blaisdell

Sandia Laboratories
P.O. Box 5800
Albuquerque, NM 87115
Attn: Doc Con for ORG 2110
J.A. Hood

Sandia Laboratories
P.O. Box 5800
Albuquerque, NM 87115
Attn: Doc Con for 3141
Sandia Rpt Col

Sandia Laboratories
P.O. Box 5800
Albuquerque, NM 87115
Attn: Div 5231, J.H. Renken

Sandia Laboratories
P.O. Box 5800
Albuquerque, NM 87115
Attn: Doc Con for ORG 1933
F. Coppage

Sandia Laboratories
P.O. Box 5800
Albuquerque, NM 87115
Attn: Doc Con for ORG 2140
R. Gregory

Sandia Laboratories
P.O. Box 5800
Albuquerque, NM 87115
Attn: Doc Con for J.V. Walker

U.S. Department of Energy
Albuquerque Operations Office
P.O. Box 5400
Albuquerque, NM 87115
Attn: Doc Con for WSSB

Central Intelligence Agency
Attn: RD/SI RM 5G48 HQ Bldg
Washington, DC 20505
Attn: A.A. Padgett

Department of Commerce
National Bureau of Standards
Washington, DC 20234
Attn: Sec Officer for Appl Rad
Div, R.C. Placious

Department of Commerce
National Bureau of Standards
Washington, DC 20234
Attn: Sec Officer for J.C.French

Aerojet Electro-Systems Co
Div of Aerojet-General Corp
P.O. Box 296
Azusa, CA 91702
Attn: T.D. Hanscome

Aerospace Corporation
P.O. Box 92957
Los Angeles, CA 90009
Attn: W.W. Willis

Aerospace Corporation
P.O. Box 92957
Los Angeles, CA 90009
Attn: I.M. Garfunkel

Aerospace Corporation
P.O. Box 92957
Los Angeles, CA 90009
Attn: L.W. Aukerman

Aerospace Corporation
P.O. Box 92957
Los Angeles, CA 90009
Attn: Library

Aerospace Corporation
P.O. Box 92957
Los Angeles, CA 90009
Attn: J. Reinheimer

Avco Research & Systems Grp
201 Lowell Street
Wilmington, MA 01887
Attn: Res Lib A830 RM 7201

BDM Corporation
7915 Jones Branch Drive
McLean, VA 22101
Attn: T.H. Neighbors

BDM Corporation
P.O. Box 9274
Albuquerque International
Albuquerque, NM 87119
Attn: D.R. Alexander

Bendix Corporation
Communication Division
East Joppa Road
Baltimore, MD 21204
Attn: Document Control

Bendix Corporation
Research Laboratories Div
Bendix Center
Southfield, MI 48075
Attn: D.J. Niehaus

Boeing Company
P.O. Box 3707
Seattle, WA 98124
Attn: Aerospace Library

Boeing Company
P.O. Box 3707
Seattle, WA 98124
Attn: C. Rosenberg 2R-00

Boeing Company
P.O. Box 3707
Seattle, WA 98124
Attn: I. Amura 2R-00

Boeing Company
P.O. Box 3707
Seattle, WA 98124
Attn: H.W. Wicklein MS 17-11

Boeing Company
P.O. Box 3707
Seattle, WA 98124
Attn: R.S. Caldwell 2R-00

Booz-Allen & Hamilton, Inc
106 Apple Street
Tinton Falls, NJ 07724
Attn: R.J. Chrisner

California Institute of Tech
Jet Propulsion Laboratory
4800 Oak Grove Drive
Pasadena, CA 91103
Attn: J. Bryden

California Institute of Tech
Jet Propulsion Laboratory
4800 Oak Grove Drive
Pasadena, CA 91103
Attn: A.G. Stanley

Charles Stark Draper Lab
555 Technology Square
Cambridge, MA 02139
Attn: R.G. Haltmaier

Charles Stark Draper Lab
555 Technology Square
Cambridge, MA 02139
Attn: P.R. Kelly

Charles Stark Draper Lab
555 Technology Square
Cambridge, MA 02139
Attn: K. Fertig

Computer Sciences Corp
201 La Veta Drive N.E.
Albuquerque, NM 87108
Attn: R.H. Dickhaut

GTE Sylvania, Inc
Electronics Systems Grp
77 A Street
Needham, MA 02194
Attn: C.A. Thornhill

GTE Sylvania, Inc
Electronics Systems Grp
77 A Street
Needham, MA 02194
Attn: J.A. Waldon

GTE Sylvania, Inc
189 B Street
Needham Heights, MA 02194
Attn: C.H. Ramsbottom

GTE Sylvania, Inc
189 B Street
Needham Heights, MA 02194
Attn: H.A. Ullman

GTE Sylvania, Inc
189 B Street
Needham Heights, MA 02194
Attn: P.B. Fredrickson

GTE Sylvania, Inc
189 B Street
Needham Heights, MA 02194
Attn: H&V Group

Harris Corporation
Harris Semiconductor Div
P.O. Box 883
Melbourne, FL 32901
Attn: C.F. Davis MS 17-220

Harris Corporation
Harris Semiconductor Div
P.O. Box 883
Melbourne, FL 32901
Attn: T.L. Clark MS 4040

Harris Corporation
Harris Semiconductor Div
P.O. Box 883
Melbourne, FL 32901
Attn: W.E. Abare MS 16-111

Hazeltine Corp
Pulaski Road
Greenlawn, NY 11740
Attn: M. Waite

Honeywell, Inc
Avionics Division
2600 Ridgeway Parkway
Minneapolis, MN 55413
Attn: R.R. Johnson A1622

Honeywell, Inc
Avionics Division
13350 U.S. Highway 19 North
St. Petersburg, FL 33733
Attn: S.H. Graff MS 725-J

Honeywell, Inc
Radiation Center
2 Forbes Road
Lexington, MA 02173
Attn: Tech Library

Hughes Aircraft
Centinela & Teale
Culver City, CA 90230
Attn: B.W. Campbell MS 6-E-110

Hughes Aircraft
Centinela & Teale
Culver City, CA 90230
Attn: K.R. Walker MS D157

Hughes Aircraft
Centinela & Teale
Culver City, CA 90230
Attn: D. Binder MS 6-D147

Hughes Aircraft
P.O. Box 92919
El Segundo Site
Los Angeles, CA 90009
Attn: E.C. Smith MS A620

Hughes Aircraft
P.O. Box 92919
El Segundo Site
Los Angeles, CA 90009
Attn: W.W. Scott MS A1080

IBM Corp
Route 17C
Owego, NY 13827
Attn: F. Frankovsky

Ion Physics Corp
South Bedford Street
Burlington, MA 01803
Attn: R.D. Evans

IRT Corp
P.O. Box 81087
San Diego, CA 92138
Attn: R.L. Mertz

IRT Corp
P.O. Box 81087
San Diego, CA 92138
Attn: R.H. Stahl

IRT Corp
P.O. Box 81087
San Diego, CA 92138
Attn: MDC

IRT Corp
P.O. Box 81087
San Diego, CA 92138
Attn: J.A. Naber

Jaycor
205 S Whiting St, Suite 500
Alexandria, VA 22304
Attn: C. Turesko

Jaycor
205 S Whiting St, Suite 500
Alexandria, VA 22304
Attn: R. Sullivan

Kaman Sciences Corp
P.O. Box 7463
Colorado Springs, CO 80933
Attn: A.P. Bridges

Kaman Sciences Corp
P.O. Box 7463
Colorado Springs, CO 80933
Attn: J.I. Lubell

Kaman Sciences Corp
P.O. Box 7463
Colorado Springs, CO 80933
Attn: D.H. Bryce

Kaman Sciences Corp
P.O. Box 7463
Colorado Springs, CO 80933
Attn: W.E. Ware

Litton Systems, Inc
Guidance & Cont Sys Div
5500 Canoga Ave
Woodland Hills, CA 91364
Attn: V.J. Ashby MS 67

Litton Systems, Inc
Guidance & Cont Sys Div
5500 Canoga Ave
Woodland Hills, CA 91364
Attn: J.P. Retzler

Lockheed Missiles & Space
P.O. Box 504
Sunnyvale, CA 94088
Attn: L. Rossi Dept 81-64

Lockheed Missiles & Space
P.O. Box 504
Sunnyvale, CA 94088
Attn: B.T. Kimura Dept 81-14

Lockheed Missiles & Space
P.O. Box 504
Sunnyvale, CA 94088
Attn: E.A. Smith Dept 85-85

Lockheed Missiles & Space
P.O. Box 504
Sunnyvale, CA 94088
Attn: P.J. Hart Dept 81-14

Lockheed Missiles & Space
P.O. Box 504
Sunnyvale, CA 94088
Attn: P.J. Hart Dept 81-14

Lockheed Missiles & Space
P.O. Box 504
Sunnyvale, CA 94088
Attn: S.I. Taimuty Dept 85-85

Lockheed Missiles & Space
3251 Hanover Street
Palo Alto, CA 94304
Attn: Tech Info Ctr D/Coll

MIT Lincoln Laboratory
P.O. Box 73
Lexington, MA 02173
Attn: L. Loughlin A-082

Martin Marietta Aerospace
P.O. Box 5837
Orlando, FL 32805
Attn: W.W. Mras MP-413

Martin Marietta Aerospace
P.O. Box 5837
Orlando, FL 32805
Attn: M.C. Griffith MP-30

Martin Marietta Corp
P.O. Box 179
Denver, CO 80201
Attn: B.T. Graham MS PO-454

Martin Marietta Corp
P.O. Box 179
Denver, CO 80201
Attn: J.R. McKee Res Lib 6617

Martin Marietta Corp
P.O. Box 179
Denver, CO 80201
Attn: J.E. Goodwin MS 0452

McDonnell Douglas Corp
P.O. Box 516
St. Louis, MO 63166
Attn: Tech Library

McDonnel Douglas Corp
5301 Bolsa Ave
Huntington Beach, CA 92647
Attn: S. Schneider

Mission Research Corp
735 State Street
Santa Barbara, CA 93101
Attn: W.C. Hart

Mission Research Corp
P.O. Box 1209
La Jolla, CA 92038
Attn: J.P. Raymond

Mission Research Corp
P.O. Box 1209
La Jolla, CA 92038
Attn: V.A.J. Van Lint

National Academy of Sciences
National Mat'ls Advisory Board
2101 Constitution Ave, NW
Washington, DC 20418
Attn: R.S. Shane

University of New Mexico
1821 Roma N.E.
Albuquerque, NM 87106
Attn: W.W. Grannemann

University of New Mexico
Electrical Engineering
Albuquerque, NM 87131
Attn: H. Southward

Northrop Corp
Electronic Division
1 Research Park
Palos Verdes Penin, CA 90274
Attn: B.T. Ahlport

Northrop Corp
Electronic Division
1 Research Park
Palos Verdes Penin, CA 90274
Attn: G.H. Towner

Northrop Corp
Research & Technology Center
3401 West Broadway
Hawthorne, CA 90250
Attn: D.N. Pocock

Northrop Corp
Research & Technology Center
3401 West Broadway
Hawthorne, CA 90250
Attn: J.R. Srour

Northrop Corp
Electronic Division
2301 West 120th Street
Hawthorne, CA 92050
Attn: V.R. DeMartino

Physics International
2700 Merced Street
San Leandro, CA 94577
Attn: Doc Con for C.H. Stallings

Physcis International
2700 Merced Street
San Leandro, CA 94577
Attn: Doc Con for J.H. Huntingtn

R&D Associates
P.O. Box 9695
Marina Del Rey, CA 90291
Attn: S.C. Rogers

Raytheon Company
Hartwell Road
Bedford, MA 01730
Attn: G.H. Joshi, Radar Sys Lab

RCA
Astro Electronics
P.O. Box 800
Princeton, NJ 08540
Attn: G.J. Brucker

RCA
Sarnoff Research Center
P.O. Box 432
Princeton, NJ 08540
Attn: K. Zaininger

Rensselaer Polytechnic Inst
P.O. Box 965
Troy, NY 12181
Attn: R.J. Gutmann

Research Triangle Institute
P.O. Box 12194
Research Triangle Park, NC27709
Attn: Sec Officer for M. Simons

Rockwell International
P.O. Box 3105
Anaheim, CA 92803
Attn: J.E. Bell HA10

Rockwell International
P.O. Box 3105
Anaheim, CA 92803
Attn: G.C. Messenger FB61

Rockwell International
P.O. Box 3105
Anaheim, CA 92803
Attn: D.J. Stevens FA70

Rockwell International
P.O. Box 3105
Anaheim, CA 92803
Attn: K.F. Hull

Rockwell International
P.O. Box 3105
Anaheim, CA 92803
Attn: N.J. Rudie FA53

Rockwell International
Collins Division
400 Collins Road NE
Cedar Rapids, IA 52406
Attn: D. Sutherland

Sanders Associates, Inc
95 Canal Street
Nashua, NH 03060
Attn: M.L. Aitel NCA 1-3236

Science Applications, Inc
P.O. Box 2351
La Jolla, CA 92038
Attn: L. Scott

Science Applications, Inc
P.O. Box 2351
La Jolla, CA 92038
Attn: J.R. Beyster

Science Applications, Inc
2109 W. Clinton Ave
Suite 700
Huntsville, AL 35805
Attn: N.R. Byrn

Science Applications, Inc
2680 Hanover Street
Palo Alto, CA 94303
Attn: C. Stevens

Science Applications, Inc
8400 Westpark Drive
McLean, VA 22101
Attn: W.L. Chadsey

Simulation Physics, Inc
P.O. Box D
Bedford, MA 01730
Attn: R.G. Little

Singer Company
150 Totowa Road
Wayne, NJ 07470
Attn: Tech Info Center

Singer Company
1150 McBride Ave
Little Falls, NJ 07424
Attn: I. Goldman

Sperry Rand Corp
Marcus Avenue
Great Neck, NY 11020
Attn: C.L. Craig

Sperry Rand Corp
Marcus Avenue
Great Neck, NY 11020
Attn: P. Maraffino

Stanford Research Institute
333 Ravenswood Ave
Menlo Park, CA 94025
Attn: P.J. Dolan

Stanford Research Institute
306 Wynn Drive, NW
Huntsville, AL 35805
Attn: M. Morgan

Sundstrand Corp
4751 Harrison Ave
Rockford, IL 61101
Attn: C.B. White

Texas Instruments, Inc
P.O. Box 5747
Dallas, TX 75222
Attn: D.J. Manus MS 72

TRW Defense & Space Sys Group
One Space Park
Redondo Beach, CA 90278
Attn: O.E. Adams R1-1144 (2)

TRW Defense & Space Sys Group
One Space Park
Redondo Beach, CA 90278
Attn: Tech Info Ctr S-1930

TRW Defense & Space Sys Group
One Space Park
Redondo Beach, CA 90278
Attn: R.M. Webb R1-2410

TRW Defense & Space Sys Group
One Space Park
Redondo Beach, CA 90278
Attn: R.K. Plebuch R1-2078
(2)

TRW Defense & Space Sys Group
One Space Park
Redondo Beach, CA 90278
Attn: H.H. Holloway R1-2036

TRW Defense & Space Sys Group
P.O. Box 1310
San Bernardino, CA 92402
Attn: R. Kitter

TRW Defense & Space Sys Group
P.O. Box 1310
San Bernardino, CA 92402
Attn: F.B. Fay

TRW Defense & Space Sys Group
P.O. Box 1310
San Bernardino, CA 92402
Attn: E.W. Allen 520/141

Vought Corp
P.O. Box 5907
Dallas, TX 75222
Attn: Tech Data Center

Westinghouse Electric
P.O. Box 1693
Baltimore-Washington Internat'l
Baltimore, MD 21203
Attn: H.P. Kalapaca MS 3525

Jet Propulsion Laboratory
California Institute of Tech
4800 Oak Grove Drive
Pasadena, CA 91103
Attn: J. Maserjian MS 198-229